Measuring the Truncation of Dark Matter Haloes with Weak Galaxy-Galaxy Lensing

The Dark Matter Haloes of Galaxies in Groups

By

Blair J. Cardigan Smith, B.Sc.

A Thesis

Submitted to the School of Graduate Studies

in Partial Fulfilment of the Requirements

for the Degree

Master of Science

McMaster University

Master of Science (2011) McMaster University

(Department of Physics and Astronomy) Hamilton, Ontario

TITLE: The Dark Matter Haloes of Galaxies in Groups

AUTHOR: Blair Cardigan Smith, B.Sc.

SUPERVISOR: Laura Parker

NUMBER OF PAGES: x, 101

Abstract

Galaxies live in extended, non-luminous haloes of dark matter. How dark matter haloes are affected by environment has been examined using cosmological simulations, and resulting predictions tested for isolated and cluster galaxies. However, predictions have have yet to be tested in the intermediate density environment of galaxy groups. We present a weak galaxy-galaxy lensing analysis of galaxies in groups, with the aim of examining how the group environment affects the dark matter haloes of member galaxies. In particular, we address three questions: 1) whether the dark matter haloes of galaxies in groups are truncated relative to galaxies in the field, 2) how dark matter is distributed within the group environment and 3) whether the halo-to-stellar mass ratio is different between field and group galaxies. We use a basic stacking method and a maximum likelihood technique to parameterize the dark matter haloes of group and field galaxies. Our samples of intermediate redshift group and field galaxies were identified by the Group Environment and Evolution Collaboration in the CNOC2 Redshift Survey. For these data, we measure the average radial extent of a group galaxy dark matter halo to be $s_* = 54^{+114}_{-39}$ kpc, which hints at the possible truncation of galaxy haloes in the group environment. We develop a method of examining the distribution of dark matter within the galaxy group itself, but obtain inconclusive results. Our preliminary analysis of star formation efficiency (halo-to-stellar mass ratio) indicates group galaxies may be less efficient at forming stars compared to galaxies in the field. Larger data samples are required in order to conduct a more rigorous analysis.

Acknowledgements

Thank you to my supervisor, Laura Parker, for you patience, guidance, inspiring intelligence and infectious enthusiasm. Thank you to my committee, Doug Welch and James Wadsley, for your insights and kind encouragements. Thank you to my friends, Brendan and Annie, for your constant help, advice and sustaining encouragement.

This work is for my family - ma, pa and sis - whom I love so dearly.

Table of Contents

List of Figures

List of Tables

Chapter 1

Introduction

The existence of dark matter was first suggested by Fritz Zwicky in the 1930s. He realized that galaxies in the Coma cluster were moving much too quickly to be held together unless there was a lot more mass present than observed (Zwicky, 1937). This idea was reinforced and popularized in the 1970s with the observation of flat galaxy rotation curves (Rubin & Ford, 1970). Given the observed distribution of stars in the Andromeda galaxy, for example, you would expect their rotational velocity to decrease with radius if light traces mass. A flat rotation curve implies much more mass at large radii than we can see.

Today, it is widely accepted that galaxies and systems of galaxies alike live in large haloes of non-luminous dark matter, yet the properties of these haloes are not fully understood. One way to study dark matter haloes is through cosmological simulations that evolve the universe from first principles in order to reproduce the structure we see today (e.g., the Millenium Simulation described by Springel et al., 2005). In doing so, simulations provide predictions regarding the nature of dark matter haloes. The picture they paint is of a universe in which structure grows hierarchically; where small dark matter haloes merge and grow over time to form larger dark matter haloes. On all scales - from the dark matter haloes of dwarf galaxies to those containing galaxy clusters - dark matter haloes appear to be of one form (e.g., Navarro et al., 2004). Their density is found to decrease steeply with increasing radius, and is well modelled by a Navarro-Frenk-White (NFW) density profile (Navarro et al., 1996, 1997).

Testing these predictions is difficult, however, because dark matter haloes cannot be observed directly. Observationally, dark matter haloes have historically been studied using dynamical methods. These include observations of globular clusters (e.g., Cohen & Ryzhov, 1997; Spitler & Forbes, 2009) or planetary nebulae (e.g., Hui et al., 1995; Romanowsky et al., 2003) and the analysis of extended rotation curves employed by Rubin & Ford (1970). Such methods are limited by the existence of visual tracers and therefore cannot be used to study dark matter haloes at radii larger than tens of kiloparsecs. As shown in Figure 1.1, the dynamics of satellite galaxies can go further; they can trace the gravitational potential of a galaxy (and therefore its dark matter halo) out to a few hundred kiloparsecs (Zaritsky & White, 1994; Conroy et al., 2005; Prada et al., 2006). With this method, the line-of-sight velocities of numerous satellite galaxies are combined in order measure the dark matter halo properties of an average host galaxy. In order to extract halo parameters, however, the systems must be assumed to be in dynamical equilibrium.

Weak galaxy-galaxy lensing is another method that, like satellite galaxy dynamics, can be used to probe the dark matter haloes of galaxies out to large radii (Figure 1.1). As a purely gravitational effect, it is not limited by the existence of visual tracers nor does it depend on the nature of matter. The major benefit of weak galaxy-galaxy lensing over satellite galaxy dynamics is that it does not rely on assumptions about the dynamical state of a galaxy.

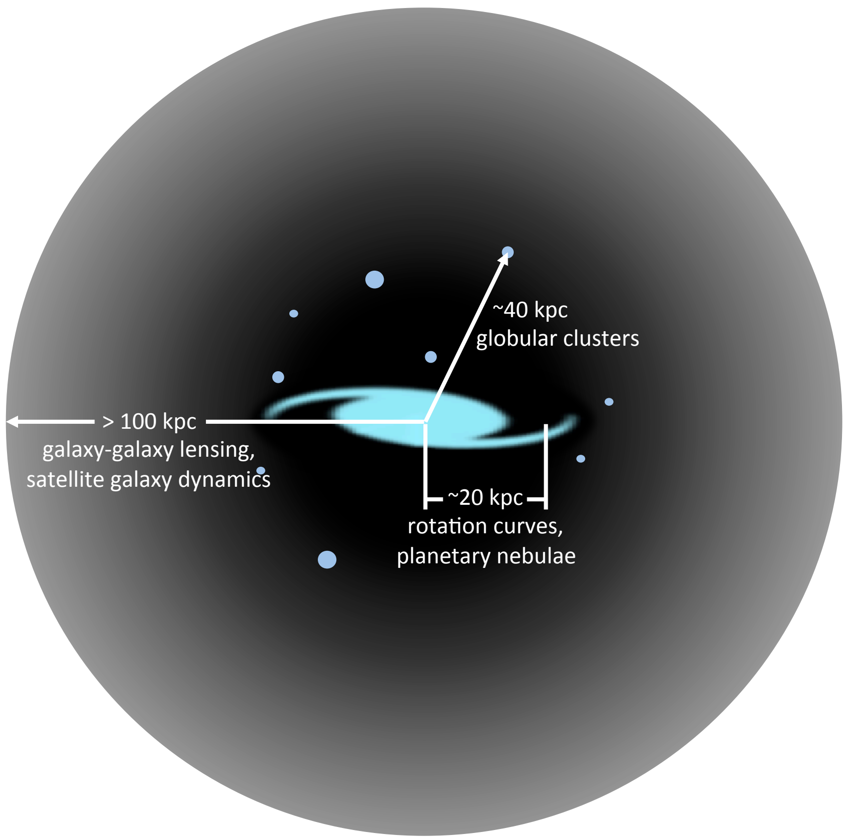

Figure 1.1: A schematic of dark matter halo tracers. Galaxy rotation curves, planetary nebulae and globular clusters can be used to trace the dark matter halo to only a few tens of kiloparsecs, while satellite galaxy dynamics and weak galaxy-galaxy lensing can probe dark matter haloes to a few hundred kiloparsecs.

Weak galaxy-galaxy lensing occurs when light from a background galaxy is deflected as it passes a foreground galaxy along the line-of-sight. This introduces coherent distortions to the images of the background galaxies. By measuring these distortions, information about the dark matter haloes of foreground galaxies - such as their mass and radial extent - can be extracted. However, the galaxy-galaxy lensing signal is so weak it cannot be detected for an individual system. The signal surrounding hundreds to thousands of foreground galaxies must be combined in order to measure weak galaxy-galaxy lensing with statistical significance (e.g., Kaiser et al., 1995; Brainerd et al., 1996; Schneider & Rix, 1997; Hudson et al., 1998; Fischer et al., 2000). As with satellite galaxy dynamics, weak galaxy-galaxy lensing can therefore only measure the average dark matter halo properties for an ensemble of foreground galaxies.[1]

It is only recently, with improved telescope technology, analysis tools and sufficiently large, high-quality datasets, that weak galaxy-galaxy gravitational lensing was detected for the first time (Brainerd et al., 1996). Since that time, however, the study of weak galaxy-galaxy lensing has grown significantly, with numerous authors reporting successful detections (e.g., Hudson et al., 1998; Hoekstra et al., 2003, 2005; Kleinheinrich et al., 2006; Limousin et al., 2007; Parker et al., 2007). Much effort has been devoted to understanding and reducing the sources of error associated with weak galaxy-galaxy lensing. For example, the importance of accurate redshift measurements has been investigated by Kleinheinrich et al. (2005), while Hoekstra et al. (2011) have analyzed the effects of large scale structure. Many authors have compared how well various dark matter halo density models - such as the NFW and singular isothermal

[1] Note, however, that weak gravitational lensing can be used to study an individual galaxy cluster (e.g. Squires et al., 1996; Smail et al., 1997). This is because an individual galaxy cluster will distort a larger number of background galaxies than an individual galaxy and, since a galaxy cluster is more massive, the distortions are larger.

sphere profiles described in Section 1.2 - fit to observations (Hoekstra et al., 2004; Limousin et al., 2005; Kleinheinrich et al., 2006; Mandelbaum et al., 2006), and examined which model parameters are most easily constrained (velocity dispersion, truncation radius, concentration, luminosity-scaling index, etc., have all been investigated; Schneider & Rix, 1997; Natarajan & Kneib, 1997; Kleinheinrich et al., 2006).

Most relevant to this work, however, are the insights weak galaxy-galaxy lensing has made regarding the effect of environment on galaxy dark matter haloes. Weak galaxy-galaxy lensing has been used to measure the dark matter haloes of galaxies in clusters (Natarajan & Kneib, 1997; Limousin et al., 2005, 2007; Natarajan et al., 2002) as well as in the field (Brainerd et al., 1996; Fischer et al., 2000; Smith et al., 2001; Hoekstra et al., 2003, 2004). Evidence suggests that as galaxies fall into the cluster system, their dark matter haloes become stripped and therefore truncated. Limousin et al. (2007), for example, find that for a galaxy with a particular luminosity, the average radial extent of the dark matter halo of a cluster galaxy is less than 50 kpc. An isolated galaxy of the same luminosity is found to have a radial extent greater than a few hundred kiloparsecs (Brainerd et al., 1996; Fischer et al., 2000; Smith et al., 2001). Such observations have been supported by simulations predicting the stripping of galaxy dark matter haloes (e.g. Ghigna et al., 1998).

Dark matter haloes have yet to be studied in the density environment intermediate to that of field and cluster galaxies; that of galaxy groups, with masses of order 10^{13} $M_\odot$. The overall theme of this thesis is to investigate how the dark matter haloes of galaxies are affected by the galaxy group environment. This task can be broken down into two goals. Following Limousin et al. (2007), we use weak galaxy-galaxy lensing to measure whether the dark matter haloes of group galaxies are truncated relative to field galaxies. We expect that this truncation should occur, though to a lesser extent than with cluster galaxies. As a further step, we examine how dark matter is distributed within a galaxy group itself; that is, what fraction of dark matter is contained within the smooth halo of the group compared to the subhaloes of individual member galaxies. Recent simulations suggest that if a large fraction of dark matter is contained within subhaloes of member galaxies, the weak galaxy-galaxy lensing signal of the smooth halo should be small compared to that of the member galaxies (Möller et al., 2002).

Although the goal of this work is primarily to measure the dark matter halo properties of galaxies in groups compared to those in the field, a next step of great importance would be to correlate dark matter halo properties with observed galaxy properties such as luminosity, morphology, stellar mass and star formation rate. To this end, we provide an initial investigation of how stellar mass relates to properties of dark matter haloes in the group and field environments. In particular, we investigate whether, the halo-to-stellar mass ratio of galaxies in groups differs from those in the field. Eventually, such analysis will provide a critical link between galaxy observations and dark matter-only cosmological simulations such as the Millennium Simulation. Understanding the link between dark and luminous material in galaxies is a critical aspect of galaxy evolution models.

1.1 Galaxy Groups

Galaxy groups represent an environment intermediate in mass and density between rich galaxy clusters and relatively isolated field galaxies, and are therefore believed to represent a transition stage between the field and cluster environment (Wilman et al., 2005; Weinmann et al., 2006; Balogh et al., 2011). Despite the fact that groups are the most common environment in the local universe (Geller & Huchra, 1983; Eke et al., 2005), relatively little is known about them in comparison to clusters or individual galaxies. This stems in large part from the fact that they are difficult to identify. Optically, the systems are not dense enough compared to background galaxies to be identified easily. This is unlike rich galaxy clusters, which appear as large over-densities of galaxies on the sky. Moreover, while galaxy clusters are characterized by extended X-ray emission, galaxy groups contain relatively little hot gas, making X-ray identification of groups difficult (Fang et al., 2007; Finoguenov et al., 2009).

Galaxy groups are typically identified by applying group-finding algorithms such as the friends-of-friends algorithm to optical data (Huchra & Geller, 1982; Carlberg et al., 2001). This algorithm links galaxies in projected position and redshift in order to identify galaxy groups, and therefore requires spectroscopic redshifts of galaxies to high completeness. Variations on the friends-of-friends algorithm requiring only photometric redshifts have been developed (e.g., the probability friends-of-friends algorithm described by Li & Yee, 2008). However, these photometric methods have large uncertainties that increase both the probability of false detection and fraction of interlopers (that is, individual galaxies falsely identified as group members) (Mamon, 2008). Once a galaxy group has been identified using photometric redshifts, it is ideal to obtain spectroscopic redshifts of individual galaxies in order to confirm the classification of an individual galaxy as 'group' or 'field.'

It is only within the last decade that large catalogues of galaxy groups have become available, allowing the properties of galaxy groups to be studied in greater detail. Catalogues have been identified using, for example, the Canadian Network for Observational Cosmology Survey (CNOC2) (Carlberg et al., 2001; Wilman et al., 2005), the Two-degree Field Galaxy Redshift Survey (2dFGRS) (Eke et al., 2004), the second Deep Extragalactic Evolutionary Probe (DEEP2) (Gerke et al., 2005) and the Sloan Digital Sky Survey (SSDS DR4) (Yang et al., 2007). From such data, the galaxies living in groups have been shown to have colour, star formation rates, and morphologies intermediate between the blue star-forming field galaxies and "red, dead" cluster galaxies (Wilman et al., 2005; Weinmann et al., 2006; Balogh et al., 2011). This evidence suggests that galaxy groups play an important role in galaxy evolution.

While much is being learned about the observable properties of galaxies in groups, the properties of their dark matter haloes remain relatively unknown. By measuring the dark matter haloes of group galaxies with weak galaxy-galaxy lensing, in this work we hope not only to study the haloes themselves, but how dark matter and observable properties are related.

1.2 Dark Matter Haloes

Whether in the field, group, or cluster environment, individual galaxies are believed to reside in extended dark matter haloes. Similarly, the group and cluster systems are themselves contained within a smooth, diffuse halo of dark matter. Cosmological simulations can be used to predict what these dark matter haloes look like. These simulations show that while dark matter haloes span over five orders of magnitude in mass, their density profiles are remarkably similar (Dubinski & Carlberg, 1991; Navarro et al., 1995, 2004).

1.2.1 Simulated Dark Matter Halo Profiles

Early simulations found that the collapse of spherical primordial overdensities resulted in structures with a single power law density profile (e.g., Fillmore & Goldreich, 1984; Bertschinger, 1985; Hoffman, 1988). With improved N-body simulations, this simple model quickly became insufficient for describing the density profiles of the cold dark matter haloes formed through hierarchical structure growth. Navarro, Frenk & White (1995, 1996, 1997) proposed representing the density profiles of dark matter haloes with a broken power law that scales as $\rho(r) \propto r^{-1}$ toward their centres and $\rho(r) \propto r^{-3}$ in outer regions. Moore et al. (1999) proposed a similar relation to describe dark matter halo density, though with an even steeper inner slope $\rho(r) \propto r^{-1.5}$ (see, e.g., Dubinski & Carlberg, 1991, for related density profiles).

The so-called NFW profile has been more widely adopted than the Moore profile, but both have been robust in modelling dark matter halo structure on all mass scales (e.g. Navarro et al., 2004). It is only recently, with the availability of higher resolution simulations, that discrepancies between simulations and these profiles have arisen (Navarro et al., 2004; Diemand et al., 2005). These discrepancies are found to increase systematically inward, indicating the need for steeper density profiles than even the the Moore profile. Merritt et al. (2005, 2006) were among the first to attempt to account for these differences by applying an Einasto profile. The Einasto profile has the functional form $\rho(r) \propto \exp(Ar^{1/n})$, where n has been found to be ~ 6, indicating a very steep inner profile. Using the Einasto profile, it is possible to model simulated data down to 0.1% of a virial radius (Diemand et al., 2005). In particular, The Einasto profile has been found to provide a better fit than NFW to the simulated dark matter haloes of galaxies (Merritt et al., 2005, 2006; Graham et al., 2006; Prada et al., 2006).

While simulations appear to be generating 'cuspy' dark matter haloes with progressively steeper inner profiles (Navarro et al., 2004; Diemand et al., 2005), observations are finding that dark matter halo profiles flatten toward inner regions (e.g., van den Bosch et al., 2000; Treu & Koopmans, 2004). Although the nature of the inner profile remains an important topic in astronomy, weak galaxy-galaxy lensing is not the best tool to probe this regime. Since weak galaxy-galaxy lensing cannot resolve the innermost regions of dark matter haloes, dynamical methods or strong gravitational lensing represent better observational means of addressing this question.

1.2.2 Observed Dark Matter Halo Profiles

While the dark matter haloes produced by simulations are well fit by NFW-like profiles, results from strong gravitational lensing studies are better fit by isothermal spheres, with $\rho(r) \propto r^{-2}$ (e.g., Treu & Koopmans, 2004). This difference likely illustrates the influence of baryons on dark matter haloes, which cannot be reproduced through dark matter-only simulations (e.g., Mashchenko et al., 2008, have shown how baryon physics can reproduce cores in dwarf galaxies). However, beyond a few kiloparsecs in radii, galaxies become dark matter dominated. In this regime, the lack of baryons means they cannot influence the dark matter halo strongly, and the NFW profile is well motivated.

Although strong gravitational lensing studies can distinguish between the various mass models, weak galaxy-galaxy lensing observations cannot. The residual from fitting an isothermal mass model is roughly equivalent to that from fitting an NFW (Hoekstra et al., 2003, 2004). Since the NFW profile has an additional parameter compared to an isothermal sphere, we will adopt isothermal sphere models for this work. Moreover, owing to the shape of observed rotation curves (e.g., Rubin & Ford, 1970), the earliest observational studies modelled the dark matter haloes of galaxies as isothermal spheres which produce flat rotation curves at large radii. The first weak galaxy-galaxy lensing studies, for example, fit a truncated isothermal sphere density profile to observed data (Brainerd et al., 1996; Schneider & Rix, 1997). By adopting isothermal sphere density profiles, it will be easier to compare our results against previous work.

Despite the fact that NFW and isothermal sphere profiles fit weak galaxy-galaxy lensing data equally well, recent work has shown that isothermal models tend to overestimate the mass of a dark matter halo. In particular, Wright & Brainerd (2000) find that for galaxy-sized dark matter haloes with an underlying NFW distribution, assuming a singular isothermal sphere can result in as much as a 60% overestimate in mass. Since this work is only concerned with a relative mass measure between field and group galaxies, such overestimates will not influence our results. Nevertheless, they are necessary to keep in mind when comparing against others.

An additional point worth mentioning is the triaxial nature of dark matter haloes. Simulations are finding that more often than not, dark matter haloes are triaxial with the most massive haloes being the least spherical (Warren et al., 1992; Jing & Suto, 2002; Bailin & Steinmetz, 2005). Observations have corroborated this halo asymmetry through, for example, the detection of anisotropic galaxy-galaxy lensing signal (Hoekstra et al., 2004; Parker et al., 2007; Oguri et al., 2010, though the former was debated by Mandelbaum et al., 2006). As depicted in Figure 1.2, an anisotropic dark matter halo will produce stronger weak galaxy-galaxy lensing signals in the regions labeled 'B' compared to those labeled 'A' (e.g., Natarajan & Refregier, 2000; Hoekstra et al., 2004; Parker et al., 2007). In order to analyze the lensing signal separately in regions 'A' and 'B', however, the dark matter halo anisotropy is assumed to be aligned with the observed galaxy shape. Howell & Brainerd (2010) show that this assumption is unreliable since the images of foreground galaxies are themselves gravitationally lensed. The observed orientation of a galaxy, and therefore its anisotropic dark matter halo, may differ dramatically from the actual orientation. While some galaxy-galaxy lensing studies have begun to adopt asymmetric dark matter haloes in order to better reproduce the observed data (Limousin et al., 2005, 2007), for this work we choose to model our dark matter haloes as spherically symmetric.

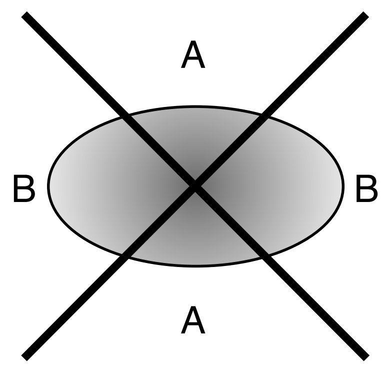

Figure 1.2: An anisotropic dark matter halo is expected to produce different weak galaxy-galaxy lensing signals in the regions labeled 'A' and 'B'.

In this work, we will use two methods of measuring weak galaxy-galaxy lensing in order to extract properties of galaxy dark matter haloes. As will be described in Chapter 2, the basic stacking method can be used to fit a one-parameter mass model to dark matter haloes, while the maximum likelihood technique can be used to measure two parameters. The one-parameter density profile we choose to adopt with the basic stacking method is the singular isothermal sphere (e.g., Kleinheinrich et al., 2005, 2006):

$$\rho_{SIS}(r) = \frac{\sigma^2}{2\pi G}\frac{1}{r^2}, \tag{1.1}$$

where G is the gravitational constant and velocity dispersion, σ, is the one free parameter. σ traces mass of the lens galaxy dark matter halo according to (Binney & Tremaine, 1987)

$$M_{SIS}(r) = \frac{2\sigma^2 r}{G}. \tag{1.2}$$

Although the singular isothermal sphere is unbounded and therefore has infinite mass, a larger σ indicates a more massive halo within a fixed radius.

With the maximum likelihood technique, we have the ability to measure two dark matter halo parameters. Since the goal of this work is to compare the radial extents of dark matter haloes in two environments - in groups and in the field - we choose to model our galaxy dark matter haloes with a truncated isothermal sphere (Brainerd et al., 1996; Hoekstra et al., 2004; Schneider & Rix, 1997; Hudson et al., 1998):

$$\rho_{TIS}(r) = \frac{\sigma^2 s^2}{2\pi G r^2 (r^2 + s^2)}, \tag{1.3}$$

where σ and truncation radius, s, are the free parameters. The mass enclosed within r in a truncated isothermal sphere is (Hoekstra et al., 2004)

$$M_{TIS}(r) = \frac{2\sigma^2 s}{G} \arctan(r/s) \tag{1.4}$$

The truncation leads to a finite total mass of (Hoekstra et al., 2003, 2004)

$$M_{tot} = \frac{\pi\sigma^2 s}{G}. \tag{1.5}$$

Alternative parameterizations could be made, but these would not help us address the question of halo truncation.

1.2.3 Dark Matter Haloes in Galaxy Groups

This smooth dark matter halo of a galaxy group is predicted to affect the dark matter (sub)haloes of individual galaxies as they fall into the system. Beyond the tidal radius, gravitational tidal forces should strip the dark matter subhaloes of satellite galaxies (Ghigna et al., 1998). Evidence corroborating this stems largely from weak galaxy-galaxy lensing studies that measure the radial extents of galaxies in the cluster system and compare these against galaxies in the field (Natarajan & Kneib, 1997; Natarajan et al., 2002; Limousin et al., 2007). If truncation of dark matter subhaloes is detected in the cluster system, we expect it should likewise occur in the group environment. However, galaxy groups contain fewer members than galaxy clusters by an order of magnitude, and have much less massive smooth dark matter haloes. Tidal forces experienced by galaxies infalling to the group system should on average be small compared to those experienced in the cluster environment. Thus, subhaloes should not be as truncated in galaxy groups as in galaxy clusters. This is illustrated schematically in Figure 1.3.

The strength of the tidal forces experienced by a galaxy in a group depend not only on the mass of the smooth group halo, but also on the distance of galaxy from the group centre. This can be understood by considering the tidal radius of a galaxy in a group. The tidal radius of a galaxy is an equilibrium point; where the gravitational force due to a galaxy is equivalent to the tidal force from the smooth group halo, and the net force is therefore zero (Binney & Tremaine, 1987). The exact size of the tidal radius depends on the mass distribution of both the galaxy halo and smooth group halo. In general, when

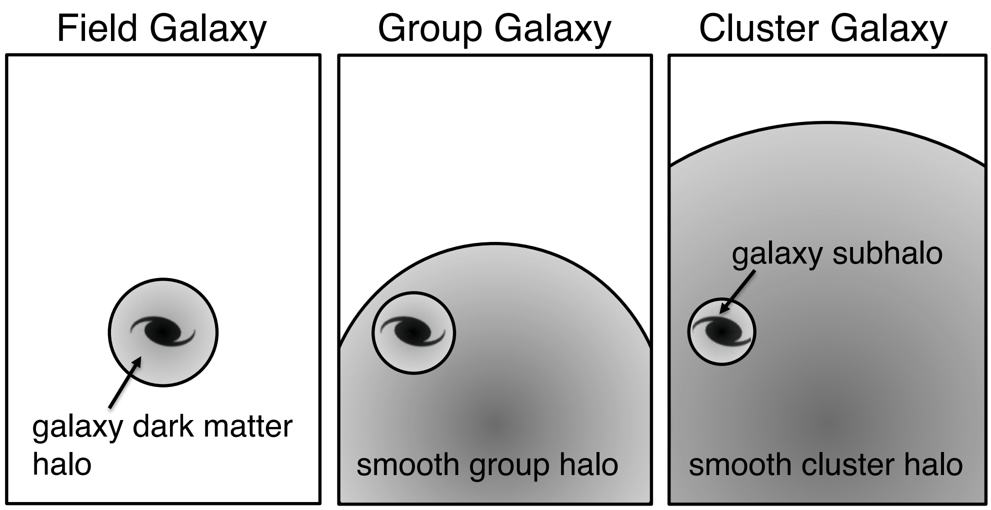

Figure 1.3: (Left panel) An isolated field galaxy (black) residing within its dark matter halo (grey). (Middle panel) The galaxy group environment is expected to truncate the dark matter subhalo (small grey) of a member galaxy due to tidal forces in the group environment (large grey represents smooth group halo), though to a lesser extent than is observed in the cluster environment (right panel).

a galaxy is close to the group centre, the tidal forces are large and the galaxy subhalo will have a very small tidal radius. Oppositely, when a galaxy is far from the group centre, the tidal forces are small, and a galaxy subhalo is expected to have a large tidal radius. How the tidal radius of a galaxy subhalo changes with distance to the group centre is shown in Figure 1.4. In this Figure, we have modelled the smooth group halo as a singular isothermal sphere and the galaxy subhalo as a truncated isothermal sphere.

A competing effect altering the profiles of dark matter subhaloes of satellite galaxies is the heating caused by tidal forces. Numerical simulations have found such heating will cause haloes to expand and therefore decrease their central density (Ghigna et al., 1998, 2000; Hayashi et al., 2003). In agreement

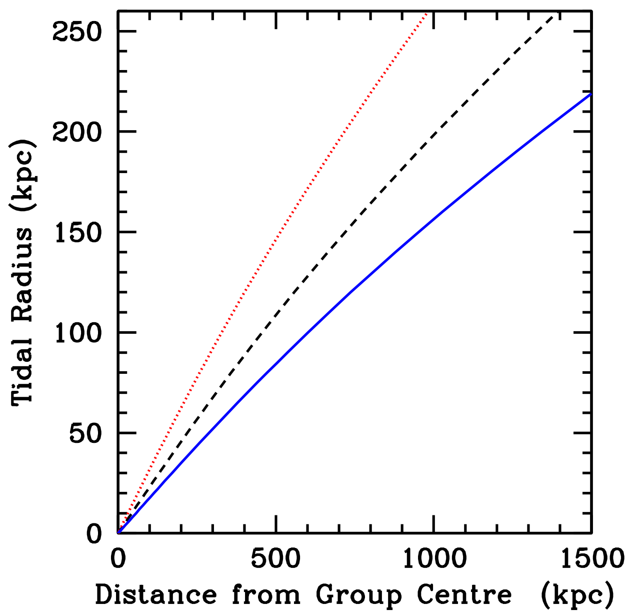

Figure 1.4: For galaxy groups of three different masses, tidal radius of a member galaxy is plotted as a function of distance of the galaxy to the group centre. The galaxy dark matter halo was modelled by a truncated isothermal sphere density profile with a total mass of 10^{12} $M_{\odot}$, velocity dispersion of 100 km s^{-1} and truncation radius of 137 kpc. The smooth group halo was modelled by a singular isothermal sphere density profile with a velocity dispersion of (dotted red) 207 km s^{-1}, (dashed black) 328 km s^{-1} and (solid blue) 464 km s^{-1}. These velocity dispersioin correspond to smooth haloes with masses of, respectively, 2×10^{13} $M_{\odot}$, 5×10^{13} $M_{\odot}$ and 1×10^{14} $M_{\odot}$ within 1 Mpc. As evident in the plot, a more massive smooth halo produces smaller tidal radii.

with this prediction, Pastor Mira et al. (2011) found no evidence of subhalo truncation in simulated galaxy clusters. Rather, the authors detected a change in concentration of dark matter subhaloes. Future work could look for changes in concentration between group and field galaxies using weak galaxy-galaxy lensing.

1.3 Thesis Objectives

This work begins with a more detailed discussion of gravitational lensing in Chapter 2. In particular, the two methods of measuring weak galaxy-galaxy lensing adopted here - namely, the basic stacking method and maximum likelihood techniques - are discussed in Sections 2.3.1 and 2.3.2, respectively. A description of our data can be found in Chapter 3, and results summarized in Chapters 4 and 5. Chapter 6 concludes this work with a discussion of these results and possible interpretations.

Bibliography

Bailin, J. & Steinmetz, M. 2005, ApJ, 627, 647

Balogh, M. L., McGee, S. L., Wilman, D. J., Finoguenov, A., Parker, L. C., Connelly, J. L., Mulchaey, J. S., Bower, R. G., Tanaka, M., & Giodini, S. 2011, MNRAS, 412, 2303

Bertschinger, E. 1985, ApJS, 58, 39

Binney, J. & Tremaine, S. 1987, Galactic dynamics, ed. Binney, J. & Tremaine, S.

Brainerd, T. G., Blandford, R. D., & Smail, I. 1996, ApJ, 466, 623

Carlberg, R. G., Yee, H. K. C., Morris, S. L., Lin, H., Hall, P. B., Patton, D. R., Sawicki, M., & Shepherd, C. W. 2001, ApJ, 552, 427

Cohen, J. G. & Ryzhov, A. 1997, ApJ, 486, 230

Conroy, C., Newman, J. A., Davis, M., Coil, A. L., Yan, R., Cooper, M. C., Gerke, B. F., Faber, S. M., & Koo, D. C. 2005, ApJ, 635, 982

Diemand, J., Zemp, M., Moore, B., Stadel, J., & Carollo, C. M. 2005, MNRAS, 364, 665

Dubinski, J. & Carlberg, R. G. 1991, ApJ, 378, 496

Eke, V. R., Baugh, C. M., Cole, S., Frenk, C. S., King, H. M., & Peacock, J. A. 2005, MNRAS, 362, 1233

Eke, V. R., Baugh, C. M., Cole, S., Frenk, C. S., Norberg, P., Peacock, J. A., Baldry, I. K., Bland-Hawthorn, J., Bridges, T., Cannon, R., Colless, M., Collins, C., Couch, W., Dalton, G., de Propris, R., Driver, S. P., Efstathiou, G., Ellis, R. S., Glazebrook, K., Jackson, C., Lahav, O., Lewis, I., Lumsden, S., Maddox, S., Madgwick, D., Peterson, B. A., Sutherland, W., & Taylor, K. 2004, MNRAS, 348, 866

Fang, T., Gerke, B. F., Davis, D. S., Newman, J. A., Davis, M., Nandra, K., Laird, E. S., Koo, D. C., Coil, A. L., Cooper, M. C., Croton, D. J., & Yan, R. 2007, ApJ, 660, L27

Fillmore, J. A. & Goldreich, P. 1984, ApJ, 281, 1

Finoguenov, A., Connelly, J. L., Parker, L. C., Wilman, D. J., Mulchaey, J. S., Saglia, R. P., Balogh, M. L., Bower, R. G., & McGee, S. L. 2009, ApJ, 704, 564

Fischer, P., McKay, T. A., Sheldon, E., Connolly, A., et al., & The SDSS Collaboration. 2000, AJ, 120, 1198

Geller, M. J. & Huchra, J. P. 1983, ApJS, 52, 61

Gerke, B. F., Newman, J. A., Davis, M., Marinoni, C., Yan, R., Coil, A. L., Conroy, C., Cooper, M. C., Faber, S. M., Finkbeiner, D. P., Guhathakurta, P., Kaiser, N., Koo, D. C., Phillips, A. C., Weiner, B. J., & Willmer, C. N. A. 2005, ApJ, 625, 6

Ghigna, S., Moore, B., Governato, F., Lake, G., Quinn, T., & Stadel, J. 1998, MNRAS, 300, 146

—. 2000, ApJ, 544, 616

Graham, A. W., Merritt, D., Moore, B., Diemand, J., & Terzić, B. 2006, AJ, 132, 2701

Hayashi, E., Navarro, J. F., Taylor, J. E., Stadel, J., & Quinn, T. 2003, ApJ, 584, 541

Hoekstra, H., Franx, M., Kuijken, K., Carlberg, R. G., & Yee, H. K. C. 2003, MNRAS, 340, 609

Hoekstra, H., Hartlap, J., Hilbert, S., & van Uitert, E. 2011, MNRAS, 412, 2095

Hoekstra, H., Hsieh, B. C., Yee, H. K. C., Lin, H., & Gladders, M. D. 2005, ApJ, 635, 73

Hoekstra, H., Yee, H. K. C., & Gladders, M. D. 2004, ApJ, 606, 67

Hoffman, Y. 1988, ApJ, 328, 489

Howell, P. J. & Brainerd, T. G. 2010, MNRAS, 407, 891

Huchra, J. P. & Geller, M. J. 1982, ApJ, 257, 423

Hudson, M. J., Gwyn, S. D. J., Dahle, H., & Kaiser, N. 1998, ApJ, 503, 531

Hui, X., Ford, H. C., Freeman, K. C., & Dopita, M. A. 1995, ApJ, 449, 592

Jing, Y. P. & Suto, Y. 2002, ApJ, 574, 538

Kaiser, N., Squires, G., & Broadhurst, T. 1995, ApJ, 449, 460

Kleinheinrich, M., Rix, H.-W., Erben, T., Schneider, P., Wolf, C., Schirmer, M., Meisenheimer, K., Borch, A., Dye, S., Kovacs, Z., & Wisotzki, L. 2005, A&A, 439, 513

Kleinheinrich, M., Schneider, P., Rix, H.-W., Erben, T., Wolf, C., Schirmer, M., Meisenheimer, K., Borch, A., Dye, S., Kovacs, Z., & Wisotzki, L. 2006, A&A, 455, 441

Li, I. H. & Yee, H. K. C. 2008, AJ, 135, 809

Limousin, M., Kneib, J. P., Bardeau, S., Natarajan, P., Czoske, O., Smail, I., Ebeling, H., & Smith, G. P. 2007, A&A, 461, 881

Limousin, M., Kneib, J.-P., & Natarajan, P. 2005, MNRAS, 356, 309

Mamon, G. A. 2008, A&A, 486, 113

Mandelbaum, R., Seljak, U., Cool, R. J., Blanton, M., Hirata, C. M., & Brinkmann, J. 2006, MNRAS, 372, 758

Mashchenko, S., Wadsley, J., & Couchman, H. M. P. 2008, Science, 319, 174

Merritt, D., Graham, A. W., Moore, B., Diemand, J., & Terzić, B. 2006, AJ, 132, 2685

Merritt, D., Navarro, J. F., Ludlow, A., & Jenkins, A. 2005, ApJ, 624, L85

Möller, O., Natarajan, P., Kneib, J.-P., & Blain, A. W. 2002, ApJ, 573, 562

Moore, B., Quinn, T., Governato, F., Stadel, J., & Lake, G. 1999, MNRAS, 310, 1147

Natarajan, P. & Kneib, J.-P. 1997, MNRAS, 287, 833

Natarajan, P., Kneib, J.-P., & Smail, I. 2002, ApJ, 580, L11

Natarajan, P. & Refregier, A. 2000, ApJ, 538, L113

Navarro, J. F., Frenk, C. S., & White, S. D. M. 1995, MNRAS, 275, 56

—. 1996, ApJ, 462, 563

—. 1997, ApJ, 490, 493

Navarro, J. F., Hayashi, E., Power, C., Jenkins, A. R., Frenk, C. S., White, S. D. M., Springel, V., Stadel, J., & Quinn, T. R. 2004, MNRAS, 349, 1039

Oguri, M., Takada, M., Okabe, N., & Smith, G. P. 2010, MNRAS, 405, 2215

Parker, L. C., Hoekstra, H., Hudson, M. J., van Waerbeke, L., & Mellier, Y. 2007, ApJ, 669, 21

Pastor Mira, E., Hilbert, S., Hartlap, J., & Schneider, P. 2011, A&A, 531, A169+

Prada, F., Klypin, A. A., Simonneau, E., Betancort-Rijo, J., Patiri, S., Gottlöber, S., & Sanchez-Conde, M. A. 2006, ApJ, 645, 1001

Romanowsky, A. J., Douglas, N. G., Arnaboldi, M., Kuijken, K., Merrifield, M. R., Napolitano, N. R., Capaccioli, M., & Freeman, K. C. 2003, Science, 301, 1696

Rubin, V. C. & Ford, Jr., W. K. 1970, ApJ, 159, 379

Schneider, P. & Rix, H.-W. 1997, ApJ, 474, 25

Smail, I., Ellis, R. S., Dressler, A., Couch, W. J., Oemler, Jr., A., Sharples, R. M., & Butcher, H. 1997, ApJ, 479, 70

Smith, D. R., Bernstein, G. M., Fischer, P., & Jarvis, M. 2001, ApJ, 551, 643

Spitler, L. R. & Forbes, D. A. 2009, MNRAS, 392, L1

Springel, V., White, S. D. M., Jenkins, A., Frenk, C. S., Yoshida, N., Gao, L., Navarro, J., Thacker, R., Croton, D., Helly, J., Peacock, J. A., Cole, S., Thomas, P., Couchman, H., Evrard, A., Colberg, J., & Pearce, F. 2005, Nature, 435, 629

Squires, G., Kaiser, N., Babul, A., Fahlman, G., Woods, D., Neumann, D. M., & Boehringer, H. 1996, ApJ, 461, 572

Treu, T. & Koopmans, L. V. E. 2004, ApJ, 611, 739

van den Bosch, F. C., Robertson, B. E., Dalcanton, J. J., & de Blok, W. J. G. 2000, AJ, 119, 1579

Warren, M. S., Quinn, P. J., Salmon, J. K., & Zurek, W. H. 1992, ApJ, 399, 405

Weinmann, S. M., van den Bosch, F. C., Yang, X., & Mo, H. J. 2006, MNRAS, 366, 2

Wilman, D. J., Balogh, M. L., Bower, R. G., Mulchaey, J. S., Oemler, A., Carlberg, R. G., Morris, S. L., & Whitaker, R. J. 2005, MNRAS, 358, 71

Wright, C. O. & Brainerd, T. G. 2000, ApJ, 534, 34

Yang, X., Mo, H. J., van den Bosch, F. C., Pasquali, A., Li, C., & Barden, M. 2007, ApJ, 671, 153

Zaritsky, D. & White, S. D. M. 1994, ApJ, 435, 599

Zwicky, F. 1937, ApJ, 86, 217

Chapter 2

Gravitational Lensing

Gravitational lensing occurs when the path of light from a distant source is deflected as it passes near a massive object. This effect can change the apparent position of the light source, as well as distort and magnify its image. Figure 2.1 shows how gravitational lensing may even cause an otherwise unobservable object - in this case, a galaxy located behind a massive object along the line-of-sight - to become observable. While the unlensed galaxy is located at an angle of θ_S from the line-of-sight, the lensed image is observed at angular position θ_I. These two quantities are related according to

$$\theta_I = \theta_S + \frac{D_{LS}}{D_S}\alpha(\theta_I), \tag{2.1}$$

where $\alpha(\theta_I)$ is the deflection angle and D_S and D_{LS} are, respectively, the cosmological angular diameter distances between the observer and source and lens and source. $\alpha(\theta_I)$ depends on the mass, M, of the lens and, more specifically, how this mass is distributed. The more mass contained within θ_I, the greater the deflection angle will be. Thus, the extent and type of distortion a background light source experiences depends on the mass distribution of the lens, the relative geometry of the lens and source on the sky, and the relative angular diameter distances of the lens and source. Reviews of gravitational lensing physics can be found in, for example, Mellier (1999) or Bartelmann & Schneider (2001).

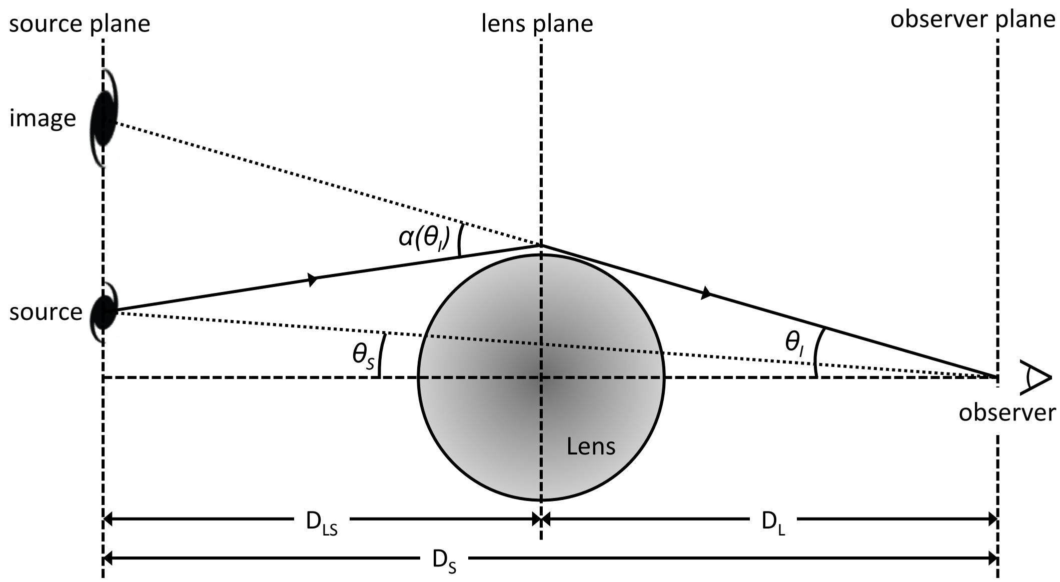

Figure 2.1: Gravitational lensing configuration of a background source galaxy (left) due to a massive lens along the line of sight. Relative to the line of sight (horizontal dashed line) of an observer (right), θ_S is the angular position of the distant galaxy in the absence of lensing and θ_I is the apparent position of its image as seen by the observer.

Since the strength of the gravitational lensing signal depends on the angular diameter distances, it is sensitive to cosmological parameters. Specifically, the density of matter in the universe, Ω_M, the density of the cosmological constant, Ω_Λ, and Hubble's constant, H_o will all effect the strength of the lensing signal. Throughout this work we adopt values of $\Omega_M = 0.3$, $\Omega_\Lambda = 0.7$ and $H_o = 70$ km s^{-1}Mpc^{-1}.

2.1 Weak versus Strong Lensing

Gravitational lensing is broken down into two regimes - weak and strong lensing - based on the extent to which the image of the light source is altered. In the regime of weak gravitational lensing, the image is only slightly distorted and the apparent position of the source on the sky does not change ($\alpha(\theta_I) = 0$, $\theta_I = \theta_S$). This is unlike strong lensing, where the apparent position of the source is changed ($\alpha(\theta_I) \neq 0$, $\theta_I \neq \theta_S$) and its image is both highly distorted and magnified. Strong gravitational lensing generates multiple images of a source. The most extreme distortion occurs when a source is imaged as a circular ring of light surrounding the lens. This form of distortion is called an Einstein ring, and occurs when the lens and source are perfectly aligned and the lens is circularly symmetric. The angular size of the ring is defined by the Einstein radius, θ_E. For a point mass M,

$$\theta_E = \left(\frac{4\pi GM}{c^2} \frac{D_{LS}}{D_L D_S} \right)^{1/2}, \tag{2.2}$$

where D_L is the angular diameter distance between the observer and lens, G the gravitational constant and c the speed of light. From this relation we see that the more massive a lens is, the larger its Einstein radius.

The Einstein radius can similarly be calculated for a singular isothermal sphere (e.g., Bartelmann & Schneider, 2001), which is a spherically symmetric mass distribution:

$$\theta_E = \frac{4\pi\sigma^2}{c^2}\beta = \left(\frac{\sigma}{186 \text{ km s}^{-1}} \right)^2 \beta \text{ arcsec} \tag{2.3}$$

where $\beta \equiv D_{LS}/D_S$ (see Figure 2.1) and σ is the velocity dispersion of the mass distribution. As discussed in Section 1.2, larger values of σ indicate more mass. This again implies that more massive objects will have larger Einstein radii.

Figure 2.2 illustrates how a background source galaxy will be gravitationally lensed in the weak and strong regimes.

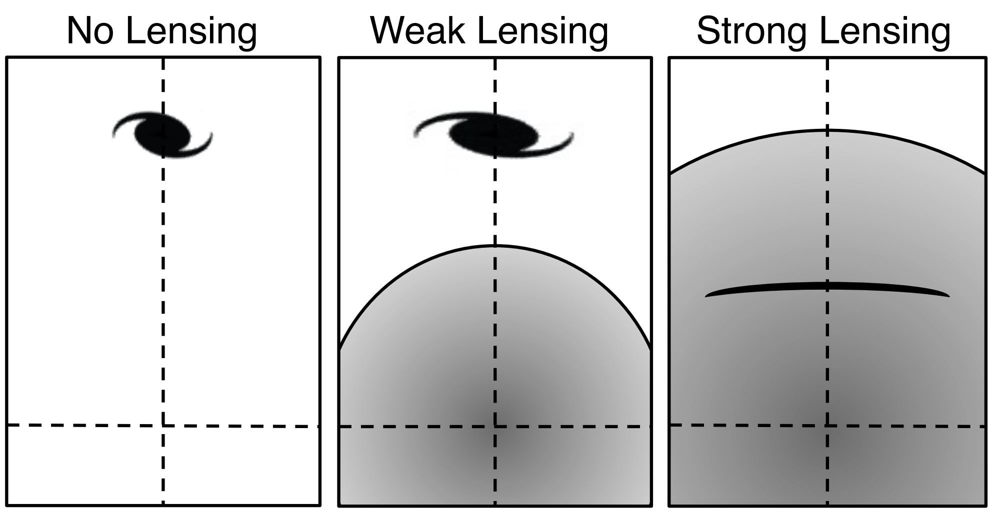

Figure 2.2: (Left panel) A view of the sky for an observer looking into the page. The image of a distant source galaxy (black) experiences no gravitational lensing - and hence no distortion - because there is no foreground mass along the line-of-sight. (Middle panel) Unless they are closely aligned, a single galaxy along the line-of-sight (grey) will only weakly lens the source; it will be stretched perpendicular to the vector connecting it to the lens, but its apparent position will remain unchanged. (Right panel) The presence of a galaxy cluster along the line-of-sight (grey) will change the apparent position of the source as well as highly distort and magnify its image. This is strong gravitational lensing. Note that the weak lensing shown here is highly exaggerated in order to make it visible.

2.2 Weak Galaxy-Galaxy Lensing

Weak galaxy-galaxy lensing occurs when the image of a background source galaxy is distorted by a foreground lens galaxy along the line-of-sight. The image of the source galaxy will be stretched perpendicular to a vector connecting it to the lens galaxy (as shown in Figure 2.2). This is called tangential shear, γ_t. Since the amount of tangential shear induced in a background galaxy will depend on the mass and distribution of the lens, by measuring γ_t it is possible to extract physical properties of the lens galaxy dark matter halo. This requires assuming a mass model such as those described in Section 1.2.

Since the shape of a background galaxy in the absence of gravitational lensing is not known, it is unfortunately not possible to measure tangential shear for an individual lens galaxy-source galaxy pair. However, it is possible to statistically measure weak galaxy-galaxy lensing for an ensemble of lens-source pairs. The more lens-source pairs available for analysis, the more statistically significant the weak galaxy-galaxy lensing measurement will be.

Number statistics are not the only factor affecting weak galaxy-galaxy lensing detections. The first attempted measurement of weak galaxy-galaxy lensing was based on over 27,800 lens-source galaxy pairs, yet Tyson et al. (1984) did not detect a gravitational lensing signal.[1] Weak galaxy-galaxy lensing was not successfully measured until 1996, when Brainerd, Blandford & Smail analyzed only 3,202 lens-source galaxy pairs. The major advantage that al-

[1] Tyson et al. (1984) (with corrections by Kovner & Milgrom, 1987) were, however, able to put an upper limit on the circular velocity of an untruncated dark matter halo at $\lesssim 330$ km s^{-1}.

lowed Brainerd et al. (1996) to detect weak galaxy-galaxy lensing while Tyson et al. (1984) could not was the superior technique used to measure background galaxy shapes. This so-called KSB method was developed by Kaiser, Squires & Broadhurst (1995) (see also Hoekstra et al., 1998).

2.3 Measuring Weak Galaxy-Galaxy Lensing

In the KSB method, the shapes of distant galaxies are described in terms of two parameters; weighted quadrupole moments e_1 and e_2 (Figure 2.3, left panel) (Kaiser et al., 1995):

$$e_1 = \frac{I_{11} - I_{22}}{I_{11} + I_{22}}, \qquad e_2 = \frac{2I_{12}}{I_{11} + I_{22}} \tag{2.4}$$

where I_{ij} are the central second moments of the galaxy image fluxes (see also Hoekstra et al., 1998). Together, e_1 and e_2 define the orientation of the galaxy on the sky and the ellipticity, e, of the galaxy, where

$$e = \sqrt{e_1^2 + e_2^2} \tag{2.5}$$

and $e \leq 1$. With these definitions, a galaxy with $e = e_1 = e_2 = 0$ is circular, whereas a galaxy with with $e = 1$ is highly elliptical.

In the absence of any foreground mass, background galaxies should be oriented randomly on the sky. If we measure the shapes of an ensemble of such galaxies, we expect to find $e_1 = e_2 = 0$ with some standard deviation, σ_e. The right panel of Figure 2.3 shows a distribution of e_1 and e_2 values for distant galaxies imaged with the Hubble Space Telescope (Hudson et al., 1998). The value of σ_e is determined by fitting a Gaussian function to the

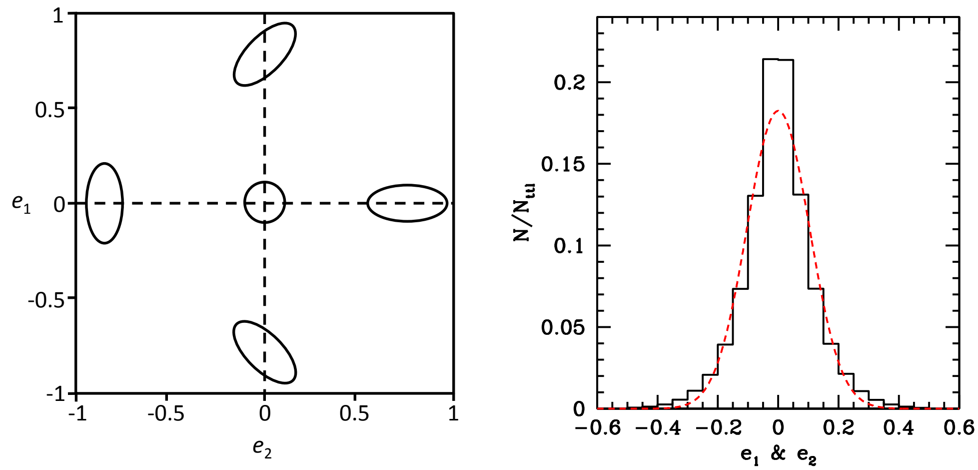

Figure 2.3: (Left) Galaxy shape parameters e_1 and e_2 define the orientation and ellipticity of a galaxy on the sky. (Right) Distribution of measured galaxy shape parameters e_1 and e_2 stacked together. The shown data is from the Canada France Hawaii Telescope Legacy Survey Deep fields. Fitting a Gaussian function (dashed red curve) to the data allows the standard deviation of the distribution, σ_e, to be measured

distribution. Typical values are $\sigma_e \approx 0.2 - 0.4$ (Brainerd et al., 1996; Hudson et al., 1998; Hoekstra et al., 2004; Kleinheinrich et al., 2005).

If a massive galaxy is located along the line-of-sight, measuring the shapes of background galaxies will yield, on average, tangential alignment of these galaxies with the foreground lens. This is caused by the stretching of the background galaxies perpendicular to the vector connecting the lens and source (Figures 2.2 and 2.4). To measure the tangential shear of a given lens-source galaxy pair, the orientation of the vector connecting the lens and source, ϕ_L, is first determined. From Figure 2.4,

$$\phi_L = \arctan\left(\frac{y}{x}\right), \tag{2.6}$$

where

$$x = -(\alpha_S - \alpha_L)\cos(\delta_L), \tag{2.7}$$

$$y = \delta_S - \delta_L, \tag{2.8}$$

and (α_L, δ_L) and (α_S, δ_S) are the right ascension and declination of the lens and source galaxies, respectively.

Using shape parameters e_1 and e_2, the orientation of the source galaxy is determined:

$$\phi_S = \frac{1}{2}\arctan\left(\frac{e_2}{e_1}\right). \tag{2.9}$$

Then,

$$e_t = -e\cos(2(\phi_S - \phi_L)), \tag{2.10}$$

where e is defined by equation (2.5) and e_t is the tangential alignment of the source galaxy with the lens. However, e_1 and e_2 are affected by the quality of the observational data. In particular, the image of a distant galaxy will be degraded by seeing and smeared due to an anisotropic point spread function (Kaiser et al., 1995). The extent to which these factors affect the measured shear is given through the shear polarizability, P_γ. Kaiser et al. (1995) describe how P_γ can be determined for each source. In general, smaller and fainter galaxies will have smaller shear polarizabilities. To correct for these effects, tangential ellipticity measurements are scaled by P_γ:

$$e_t = -\frac{e}{P_\gamma}\cos(2(\phi_S - \phi_L)). \tag{2.11}$$

The tangential shear induced with weak galaxy-galaxy lensing corresponds to a change in the shape of a background source galaxy of only a few percent

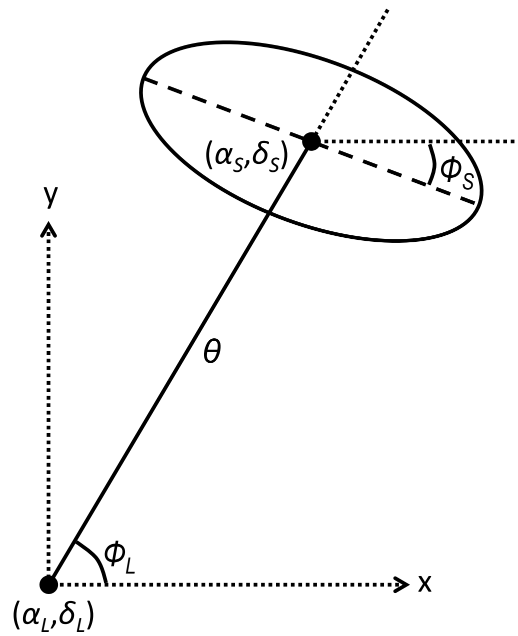

Figure 2.4: Orientation of a background source galaxy (ellipse in upper right) on the sky relative to a foreground lens galaxy (point in lower left) for an observer located out of the page. θ defines the angular separation on the sky between lens and source, whereas ϕ_L defines the orientation of this vector relative to the x-axis. The major axis of the source is shown with the dashed line, and ϕ_S defines its orientation relative to the x-axis. (α_L, δ_L) and (α_S, δ_S) are the right ascension and declination of the lens and source, respectively.

(e.g., Brainerd et al., 1996). If the ellipticity of a galaxy is $e = 0.6$ in the absence of lensing, a foreground lens galaxy may cause an observer to measure $e = 0.61$ instead. Thus, tangential shear is more than an order of magnitude smaller than the intrinsic spread in shape measurements, $\sigma_e \approx 0.3$. The signal surrounding hundreds to thousands of lens galaxies must therefore be combined in order to overcome σ_e, and measure weak galaxy-galaxy lensing with statistical significance.

2.3.1 Basic Stacking Method

The basic stacking method represents the simplest way to combine the weak galaxy-galaxy lensing signals from numerous lens-source pairs and, in essence, is the method Brainerd et al. (1996) used when they first successfully detected weak galaxy-galaxy lensing (see also Hudson et al., 1998; Hoekstra et al., 1998, 2003; Parker et al., 2007).

Combining Lens-Source Pairs

For each identified lens-source pair, the tangential ellipticity, e_t, of the background source galaxy is calculated using equation (2.11). Each e_t measurement is then binned according to the angular separation on the sky, θ, between lens and source. Within each bin, the mean tangential shear, $\langle\gamma_t\rangle$, is calculated by weighting each value of e_t by the uncertainty in the source ellipticity measurement (Hudson et al., 1998; Parker et al., 2007):

$$\langle\gamma_t\rangle = \frac{\sum\limits_i e_{t,i} w_i}{\sum\limits_i w_i}, \tag{2.12}$$

where the sum is over the number of lens-source pairs in that bin, and w is the weight of each source. As in Hoekstra et al. (2000), the weight of each source is

$$w = \frac{(P_\gamma/4)^2}{P_\gamma^2 + \Delta e^2}, \tag{2.13}$$

where Δe is the uncertainty in the galaxies measured shape. Weighting e_t values in this way effectively decreases the significance of sources with poorly defined shapes or large uncertainties due to instrumentals.

This stacking process allows $\langle\gamma_t\rangle$ to be plotted as a function of θ. The top panel of Figure 2.5 shows an example tangential shear profile from Parker et al. (2007), obtained for a sample of galaxies in the Canada France Hawaii Telescope Legacy Survey[2] (CFHTLS) Wide fields.

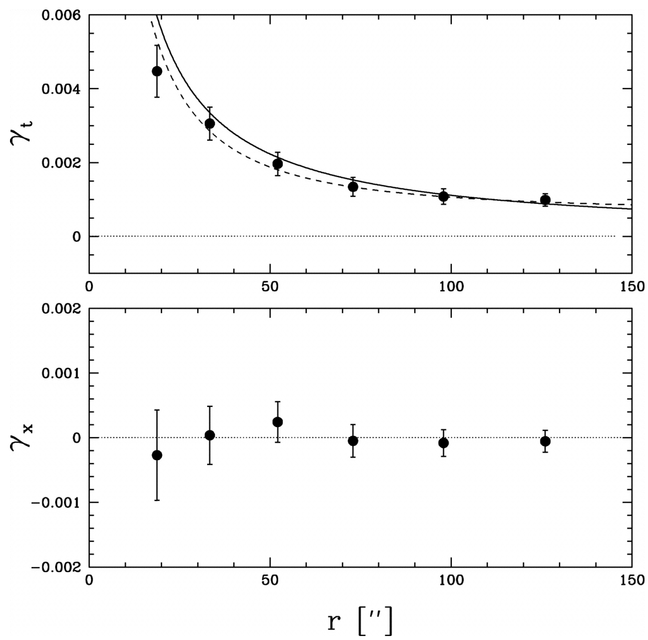

Figure 2.5: From Parker et al. (2007). (Top) The tangential shear profile obtained from basic stacking analysis of a sample of galaxies in the CFHTLS-Wide fields. The profile is fit with both singular isothermal sphere (solid line) and NFW (dashed) density profiles. The best-fit isothermal sphere has an Einstein radius of 0.24 ± 0.02, which corresponds to a velocity dispersion of 132 ± 10 km s^{-1}. For these data, the NFW profile appears to yield a slightly better fit. Over numerous lensing studies and various datasets, however, the NFW and singular isothermal sphere profiles have been found to fit observed data equally well. (Bottom) The cross-shear profile obtained when when the source images are rotated by 45°. As described in Section 4.1.1, no cross-shear signal is expected if the observed tangential shear is due to gravitational lensing.

[2] http://www.cfht.hawaii.edu/Science/CFHLS/

Adopted Dark Matter Halo Model

A one parameter mass model can be fit to the tangential shear profile. As described in Section 1.2, we choose to model the data with a singular isothermal sphere density profile. For a singular isothermal sphere (Kleinheinrich et al., 2005; Parker et al., 2007)

$$\gamma_t = \frac{\theta_E}{2\theta}. \tag{2.14}$$

θ_E is the Einstein radius of the best fitting singular isothermal sphere, and can be measured from the tangential shear profile. Making use of equation (2.3), velocity dispersion can then be calculated according to

$$\sigma = 186 \text{ km s}^{-1}\sqrt{\frac{\theta_E}{\beta}}, \tag{2.15}$$

where θ_e is measured in arcseconds. In order to calculate $\beta \equiv D_{LS}/D_S$, the weighted mean source redshift $\langle z_S \rangle$ and weighted mean lens redshift $\langle z_L \rangle$ are determined analogously to equation (2.12). These values are then used to calculate the angular diameter distances as defined by Hogg (1999) (see his equations 18 and 19).

Luminosity Scaling

In order to compare measured values of σ against literature values, results must be scaled to the velocity dispersion σ_* of an L^*-galaxy. We adopt the scaling relation

$$\left(\frac{\sigma}{\sigma_*}\right)^\eta = \frac{L(z)}{L^*(z)} = 10^{-0.4(\mu(z)-\mu^*(z))}, \tag{2.16}$$

where $\mu(z)$ is the absolute magnitude of a galaxy at a redshift of z, $\mu^*(z)$ the absolute magnitude of an L^*-galaxy at a redshift of z, and η the Faber-Jackson index analog (e.g., Brainerd et al., 1996; Schneider & Rix, 1997; Natarajan & Kneib, 1997; Hudson et al., 1998; Natarajan et al., 2002; Hoekstra et al., 2003; Kleinheinrich et al., 2005; Parker et al., 2007).

The adopted value of $\mu^*(z)$ will depend on both the filter band and redshift. We take $\mu^*_{R_c}(z = 0.4) = -20.42$ at a redshift of $z_L = 0.4$. This redshift was chosen because k-corrections to $z_L = 0.4$ were available for our data (see Chapter 3). When k-corrections were not available, we mildly evolved R_c-band absolute magnitudes according to

$$\mu_{R_c}(z = 0.4) = \mu_{R_c}(z) + 0.3 \log\left(\frac{1+z}{1.4}\right). \tag{2.17}$$

The value of $\mu^*_{R_c}$ was obtained from Lin et al. (1999), who derived the luminosity function for a sample of galaxies in the second Canadian Network for Observational Cosmology[3] (CNOC2) Redshift Survey. The authors obtained luminosity function fits at $z = 0.3$ for early, intermediate, and late type galaxies individually. We assume the same relative galaxy populations as Lin et al. (1999), allowing us to obtain a single value of $\mu^*_{R_c}$ at $z = 0.3$. This was then evolved according to equation (2.17) to $z = 0.4$.

There has been much literature debate regarding the environmental dependence of scaling relations such as equation (2.16) (e.g., Gavazzi et al., 1996; Shen et al., 2003; Kauffmann et al., 2003; Desroches et al., 2007; van den Bergh, 2008). The most recent evidence appearing to support scaling rela-

[3] http://www.astro.utoronto.ca/∼cnoc/cnoc2.html

tions that do not depend on environment (Nair et al., 2010).[4] Previous weak galaxy-galaxy lensing studies have attempted to constrain such scaling relations. In particular, the value of the index η used in equation (2.16) has been examined for numerous datasets (e.g., Hudson et al., 1998; Smith et al., 2001; Kleinheinrich et al., 2005). Kleinheinrich et al. (2005) additionally investigate how η varies with galaxy type. The authors use a maximum likelihood technique to constrain η for red and blue galaxies, separately. For both samples, the authors find galaxies to be equally well modeled by $\eta = 3.5 - 4.5$. Unless otherwise stated, we will therefore adopt a value of $\eta = 4$ in this work.

2.3.2 Maximum Likelihood Technique

The maximum likelihood technique described here was first used by Schneider & Rix (1997) to statistically quantify the shear induced by galaxy-galaxy lensing (see also, e.g., Hudson et al., 1998; Hoekstra et al., 2004; Kleinheinrich et al., 2006). This method has an advantage over the basic stacking method in that it can be used to simultaneously constrain two parameters of a dark matter halo mass model.[5] The maximum likelihood technique also accounts for multiple deflections of background galaxies, and therefore models source galaxy shapes more accurately than the basic stacking method (Brainerd et al.,

[4] Note that while the luminosity-size relationship, for example, does not appear to depend on environment, the scatter about the relationship does. Nair et al. (2010) observe scatter to increase with later Hubble types.

[5] In reality, the maximum likelihood technique can be used to constrain any number of parameters. However, the more parameters in the adopted mass model, the more computationally expensive the analysis becomes.

1996). Details of the maximimum likelihood analysis described below can be found in, for example, Schneider & Rix (1997); Hudson et al. (1998); Hoekstra et al. (2000, 2003); Kleinheinrich et al. (2005, 2006).

Combining Lens-Source Pairs

With the maximum likelihood technique, a chosen mass model is applied to all lens galaxies. This allows the tangential shear, $\gamma_{t,ij}$, that each foreground galaxy j induces in each background source galaxy i to be determined. Using $\gamma_{t,ij}$, it is possible to predict the shape source galaxy i would have in the absence of foreground galaxy j:

$$e^{(p)}_{t,ij} = e^{(o)}_{t,ij} - \gamma_{t,ij} P_\gamma \tag{2.18}$$

where $e^{(o)}_{t,ij}$ is the observed shape of source galaxy i measured tangential to lens galaxy j (equation 2.10) and $e^{(p)}_{t,ij}$ is the predicted shape.

Since multiple foreground galaxies may lens a background source galaxy, the intrinsic shape $e^{(i)}_i$ of background galaxy i is given by summing the predicted tangential shape over all lens galaxies within $\theta_{min} \leq \theta \leq \theta_{max}$:[6]

$$e^{(i)}_i = \sum_j e^{(p)}_{t,ij} = \sum_j \left(e^{(o)}_{t,ij} - \gamma_{t,ij} P_{\gamma,i} \right) \tag{2.19}$$

Strictly speaking, this expression for intrinsic shape is not exact since the shear contributions from multiple deflections do not add linearly (e.g., Blandford & Narayan 86). However, all shear contributions due to weak galaxy-galaxy lensing are small, making it possible to use equation (2.19).

[6] See Chapter 3 for details.

The best fitting mass model is that which produces source galaxies with intrinsic ellipticities that are oriented randomly on the sky. This is equivalent to saying that on average, the difference equation (2.19) is zero. Since the distribution of background source galaxies in the absence of lensing is a Gaussian function with width σ_e, the probability that the mass model in question best reproduces the tangential shear of source i is

$$P(e_i^{(i)}) = \frac{1}{\sqrt{2\pi}\sigma_e} \exp\left(-\frac{\left|e_i^{(i)}\right|^2}{2\sigma_{ttl,i}^2}\right), \tag{2.20}$$

where $\sigma_{ttl,i}^2 = \sigma_e^2 + \Delta e_i^2$, and Δe_i is the error in the shape measurement. The "likelihood" of the mass model is obtained by multiplying the probabilities of all sources:

$$Ł = \prod_i P(e_i^{(i)}) = \prod_i \frac{1}{\sqrt{2\pi}\sigma_e} \exp\left(-\frac{\left|e_i^{(i)}\right|^2}{2\sigma_{ttl,i}^2}\right). \tag{2.21}$$

Due to its relation to χ^2 (see the discussion of uncertainty below), however, the log-likelihood is more commonly computed:

$$\ell \equiv \ln Ł \propto \sum_i \left(\frac{-\left|e_i^{(i)}\right|^2}{2\sigma_{ttl,i}^2}\right) \tag{2.22}$$

The dark matter halo mass model which maximizes likelihood (and therefore log-likelihood) is the best fitting halo.

Adopted Dark Matter Halo Model

As with Schneider & Rix (1997), we adopt the truncated isothermal sphere density profile described in Section 1.2. For a truncated isothermal sphere, the tangential shear γ_t that a lens galaxy will induce in background source galaxy is

$$\gamma_t = \frac{\pi D_L \beta \sigma^2}{c^2 s} \mathrm{G}(X), \tag{2.23}$$

where $\mathrm{G}(X)$ is dimensionless and given by

$$\mathrm{G}(X) = \frac{(2+X)\sqrt{1+X^2} - 2 - X^2}{X^2\sqrt{1+X^2}}, \tag{2.24}$$

and $X = D_L\theta/s$ is also dimensionless. As before, D_L is the angular diameter distance to the lens and θ the angular lens-source separation (Schneider & Rix, 1997; Hudson et al., 1998; Hoekstra et al., 2003). Here, σ and s are the free parameters that can be varied in order to produce the lens galaxy mass model which best fits the data.

Luminosity Scaling

As with the basic stacking method, best fitting σ and s values must be scaled according to those of an L^*-galaxy, σ_* and s_*. We again use equation (2.16) in order to scale velocity dispersion, while adopting

$$\left(\frac{s}{s_*}\right)^2 = \frac{M}{M^*}, \tag{2.25}$$

where M is the dark matter halo mass, and M^* the dark matter halo mass of an L^*-galaxy Brainerd et al. (1996). If we then assume a constant M/L ratio (Brainerd et al., 1996; Schneider & Rix, 1997),

$$\left(\frac{s}{s_*}\right)^2 = \frac{L}{L^*} = \left(\frac{\sigma}{\sigma_*}\right)^\eta. \tag{2.26}$$

With these scaling relations, we can redefine tangential shear as

$$\gamma_t = \frac{\pi D_L \beta \sigma_*^2}{c^2 s_*} \left(\frac{L}{L^*}\right)^{(2/\eta - 1/2)} \mathrm{G}(X), \tag{2.27}$$

where G(X) is defined as in equation (2.24) and

$$X = \frac{D_L \theta}{s_*} \left(\frac{L^*}{L} \right)^2 . \tag{2.28}$$

Thus, the input parameters with the maximum likelihood technique are the velocity dispersion and truncation radius of an L^* galaxy, (σ_*, s_*). The dark matter halo applied to each foreground lens galaxy (σ, s) is scaled according to the luminosity of the lens. The luminosity scaling is determined as in the basic stacking method; using $L(z)/L^*(z) = 10^{-0.4(\mu(z)-\mu^*(z))}$ and $\mu^*_{R_c}(z = 0.4) = -20.42$.

In practice, likelihood (or log-likelihood) is evaluated for many pairs of σ_* and s_* values. Example results are shown in Figure 2.6, where contours represent the 1-σ, 2-σ, 3-σ and 4-σ confidence levels in the best fit solution.

Uncertainty

The uncertainty in a given mass model is determined by computing the χ^2 of the model, which we will denote by χ^2_{model}. As in Schneider & Rix (1997), this is done by conducting a likelihood ratio test (see also Hudson et al., 1998). The likelihood ratio test determines how well a set of parameters fit to the data by comparing the results to a "null model"; that is, a model where the input parameters are null. Physically, this null model corresponds to fitting all lens galaxies with dark matter haloes of zero mass. If the chosen model parameters fit the data well, then the residual of the fit should be smaller than the residual of fitting the null - i.e., no - model (e.g. Wilks, 1938).

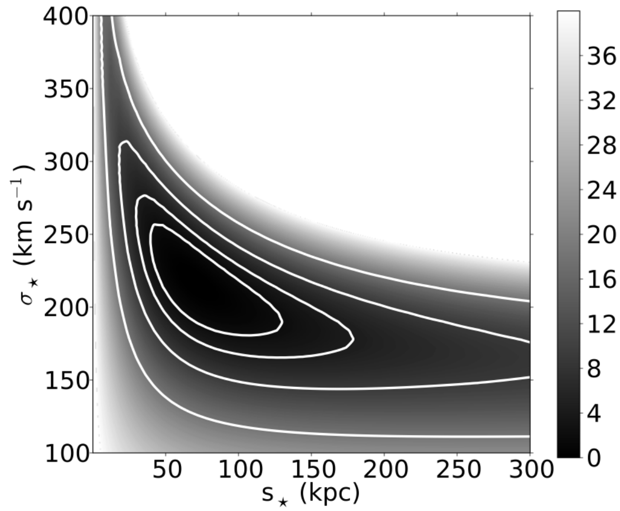

Figure 2.6: Maximum likelihood contours obtained for a sample of galaxies in the second Canadian Network for Observational Cosmology Redshift Survey. Truncation radius, s_*, is plotted against velocity dispersion, σ_*. Each (s_*, σ_*)-coordinate in the plot represents a dark matter halo mass model parameterized by σ_* and s_*. The maximum likelihood technique is used to evaluate the goodness-of-fit for each (s_*, σ_*)-pair. For the data shown, the best-fit parameters are $\sigma_* = 214^{+45}_{-33}$ km s^{-1} and $s_* = 72^{+52}_{-39}$ kpc. The colour gradient is used to indicate goodness-of-fit, where black represents a well-fitting dark matter halo, and white a poor. In order to highlight the best fitting dark matter haloes, the colour gradient has only been applied to models with $\chi^2_{model} \leq 40$. Models with $\chi^2_{model} > 40$ have all been coloured white. The contours represent the 1-σ, 2-σ, 3-σ and 4-σ confidence intervals on the best-fit solution.

With the likelihood ratio test, the goodness of fit of a given model is compared to a null model through the test statistic D:

$$D = -2\left[\ln(\text{likelihood of null model}) - \ln(\text{likelihood of model})\right]. \tag{2.29}$$

The probability distribution of D can be approximated by a χ^2-distribution with number of degrees of freedom equal to the difference in degrees of freedom between the model and null model.

For our mass model, the null model is obtained by setting $\sigma_* = 0$. This is equivalent to setting $\gamma_t = 0$. For the likelihood function in equation (2.22),

$$D = -2\left[\ell_{null} - \ell_{model}\right] = \sum_i \frac{1}{\sigma^2_{ttl,i}} \left[\left|e_i^{(o)}\right|^2 - \left|e_i^{(i)}\right|^2\right]. \tag{2.30}$$

where again, $e_i^{(i)}$ the intrinsic ellipticity of the source galaxy, and $e_i^{(o)}$ is the observed ellipticity obtained when $\gamma_{t,ij} = 0$ in equation (2.19):

$$e_i^{(o)} = \sum_j e_{t,ij}^{(o)} \tag{2.31}$$

As already stated, the best fitting dark matter halo is that which minimizes the log-likelihood ℓ_{model}. This is also the model which will maximize the test statistic D. The goodness of fit of a particular model is given by

$$\chi^2_{model} = D_{max} - D_{model}. \tag{2.32}$$

Since the dark matter halo mass model has two free parameters, σ_* and s_*, whereas the null model has zero, there are two degrees of freedom in the χ^2-distribution traced by D.[7] Thus, when $\chi^2_{model} = 2.30$, 4.61, 9.21 and 18.41, this corresponds to the 1-, 2-, 3-, and 4-σ levels of confidence in the best fitting mass model (Wall & Jenkins, 2003). These contours can be seen in Figure 2.6.

The error in the best fitting dark matter halo mass model is obtained by taking the upper and lower bounds of the 1-σ confidence levels. In the left panel of Figure 2.6, for example, while the best fitting σ_* value is 214, the σ_* values of the 1-σ contour range from 181 to 259. The best fitting dark matter

[7] Number of free parameters should not be confused with degrees of freedom. For both the model and null model, the total degrees of freedom are equal to the number of pairs plus the number of free parameters.

halo thus has $\sigma_* = 214^{+45}_{-33}$ km s^{-1}. Similarly, the truncation radius is found to be $s_* = 72^{+52}_{-39}$ kpc.

2.3.3 Smooth Halo Contribution

When considering a source galaxy located behind a galaxy group located along the line of sight, the source galaxy will experience tangential shear due not only to the subhaloes of member galaxies, but also the smooth halo of a galaxy group. This scenario is depicted in Figure 2.7. In order to determine how dark matter is distributed within galaxy groups, it is possible to measure the relative contribution of the smooth halo to the weak galaxy-galaxy lensing signal. This is done by performing maximum likelihood analysis on group galaxies with and without taking the smooth halo into account. The procedure followed when the smooth halo is not accounted for was just described in Section 2.3.2. The smooth halo is accounted for by first modelling it with a singular isothermal sphere (equation 2.14). Maximum likelihood analysis is then repeated, except we replace equation (2.18) by

$$e^{(p)}_{t,ij} = e^{(o)}_{t,ij} - \gamma_{t,ij} P_\gamma - \gamma_{tg,ij} \tag{2.33}$$

where $\gamma_{tg,ij}$ is the tangential shear that source galaxy i experiences due to the smooth group halo at the location of foreground galaxy j.

By accounting for the smooth halo in this way, it is possible to determine how much matter is contained within the individual subhaloes of member galaxies compared to the smooth group halo. If the dark matter in a group is contained mostly within the smooth halo, we expect maximum likelihood

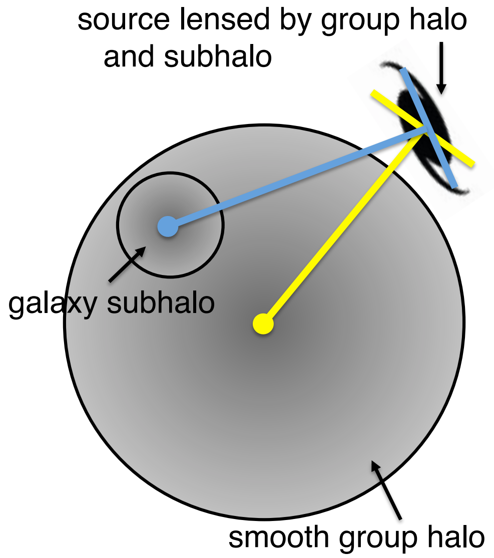

Figure 2.7: A background source galaxy (black) experiences tangential shear due to the smooth dark matter halo of a galaxy group located along the line-of- sight (large grey), as well as the subhalo of a member galaxy (small grey). The source galaxy shown here is more aligned with the galaxy subhalo than the group halo, indicating that a lot of mass must be contained within the subhalo. A less massive subhalo would lens the source only slightly compared to the smooth group halo, resulting in the source being more aligned with the group halo.

analysis to change when the group halo contribution to weak lensing is considered. Although we would ideally like to use this method to constrain the parameters of the smooth group halo, in practice our datasets are not large enough. The smooth halo contribution will only be investigated for galaxy groups with known velocity dispersions. As before, the only free parameters in equation (2.33) are σ_* and s_* of the galaxy dark matter halo.

Bibliography

Bartelmann, M. & Schneider, P. 2001, Phys. Rep., 340, 291

Brainerd, T. G., Blandford, R. D., & Smail, I. 1996, ApJ, 466, 623

Desroches, L.-B., Quataert, E., Ma, C.-P., & West, A. A. 2007, MNRAS, 377, 402

Gavazzi, G., Pierini, D., & Boselli, A. 1996, A&A, 312, 397

Hoekstra, H., Franx, M., & Kuijken, K. 2000, ApJ, 532, 88

Hoekstra, H., Franx, M., Kuijken, K., Carlberg, R. G., & Yee, H. K. C. 2003, MNRAS, 340, 609

Hoekstra, H., Franx, M., Kuijken, K., & Squires, G. 1998, ApJ, 504, 636

Hoekstra, H., Yee, H. K. C., & Gladders, M. D. 2004, ApJ, 606, 67

Hogg, D. W. 1999, ArXiv Astrophysics e-prints

Hudson, M. J., Gwyn, S. D. J., Dahle, H., & Kaiser, N. 1998, ApJ, 503, 531

Kaiser, N., Squires, G., & Broadhurst, T. 1995, ApJ, 449, 460

Kauffmann, G., Heckman, T. M., White, S. D. M., Charlot, S., Tremonti, C., Peng, E. W., Seibert, M., Brinkmann, J., Nichol, R. C., SubbaRao, M., & York, D. 2003, MNRAS, 341, 54

Kleinheinrich, M., Rix, H.-W., Erben, T., Schneider, P., Wolf, C., Schirmer, M., Meisenheimer, K., Borch, A., Dye, S., Kovacs, Z., & Wisotzki, L. 2005, A&A, 439, 513

Kleinheinrich, M., Schneider, P., Rix, H.-W., Erben, T., Wolf, C., Schirmer, M., Meisenheimer, K., Borch, A., Dye, S., Kovacs, Z., & Wisotzki, L. 2006, A&A, 455, 441

Kovner, I. & Milgrom, M. 1987, ApJ, 321, L113

Lin, H., Yee, H. K. C., Carlberg, R. G., Morris, S. L., Sawicki, M., Patton, D. R., Wirth, G., & Shepherd, C. W. 1999, ApJ, 518, 533

Mellier, Y. 1999, ARA&A, 37, 127

Nair, P. B., van den Bergh, S., & Abraham, R. G. 2010, ApJ, 715, 606

Natarajan, P. & Kneib, J.-P. 1997, MNRAS, 287, 833

Natarajan, P., Kneib, J.-P., & Smail, I. 2002, ApJ, 580, L11

Parker, L. C., Hoekstra, H., Hudson, M. J., van Waerbeke, L., & Mellier, Y. 2007, ApJ, 669, 21

Schneider, P. & Rix, H.-W. 1997, ApJ, 474, 25

Shen, S., Mo, H. J., White, S. D. M., Blanton, M. R., Kauffmann, G., Voges, W., Brinkmann, J., & Csabai, I. 2003, MNRAS, 343, 978

Smith, D. R., Bernstein, G. M., Fischer, P., & Jarvis, M. 2001, ApJ, 551, 643

Tyson, J. A., Valdes, F., Jarvis, J. F., & Mills, Jr., A. P. 1984, ApJ, 281, L59 van den Bergh, S. 2008, A&A, 490, 97

Wall, J. V. & Jenkins, C. R. 2003, Practical Statistics for Astronomers

Wilks, S. S. 1938, The Annals of Mathematical Statistics, 9, 60

Chapter 3

Data

The basic requirements for weak galaxy-galaxy lensing studies are images of reasonable quality and depth. Deeper images will contain more background galaxies, resulting in a greater number of lens galaxy-source galaxy pairs. This improves the weak galaxy-galaxy lensing statistics, allowing dark matter halo parameters to be more accurately measured. With deeper images of higher angular resolution, the shapes of background galaxies can be measured more precisely and tangential shear can be measured more accurately. However, it is the number of lens-source pairs that tends to dominate the error budget with weak galaxy-galaxy lensing.

In this work I will measure weak galaxy-galaxy lensing for two data samples described below. One sample is used exclusively for testing the adopted methods, and the other for a detailed comparison of dark matter halo properties of group and field galaxies.

3.1 CFHTLS-Deep

The Canada France Hawaii Telescope Legacy Survey[1] (CFHTLS) Deep Fields consist of four $1° \times 1°$ fields of MegaCam imaging in the (u^*, g', r', i', z') filters. Large catalogues of galaxies have been identified in these data, with photometric redshifts and absolute magnitudes measured by Ilbert et al. (2006). The shape of each galaxy was measured by Ludovic van Waerbeke using the method of Kaiser et al. (1995) (see also Hoekstra et al., 1998).[2]

From these catalogues, foreground lens galaxies were defined as having redshifts $0.2 \leq z_L \leq 1$ and apparent magnitudes $i' \leq 24.5$. In order to classify lens galaxies as residing in either the field or group environment, the probability friends-of-friends analysis (Li & Yee, 2008) previously performed by Rachel Anderson was used (Anderson, 2009). This analysis yielded a catalogue of galaxy groups with anywhere from 2 to 25 members. Without spectroscopic redshifts, these groups could not be confirmed. However, the method was calibrated on galaxies in the Millenium Simulation (Springel et al., 2005). It was found that when the number of members in a group is small, the fraction of falsely identified groups is high. Moreover, the fraction of interlopers within each group increases with decreasing number of members (Li & Yee, 2008). We therefore consider only groups with 10 or more members as real, while classifying any galaxies in groups with fewer than 6 members as isolated field galaxies. Although these restrictions increase the probability that an individual galaxy is correctly classified as a 'field' or 'group' galaxy, there is still uncertainty at approximately the 20% level (Anderson, 2009). As consequence, the CFHTLS-

[1] http://www.cfht.hawaii.edu/Science/CFHLS/

[2] See Chapter 2 for more details.

Deep catalogues cannot be used for an in-depth comparison of field and group galaxy dark matter haloes. However, the vast sizes of the catalogues make them ideal for testing methodology.

For every identified field and group lens galaxy, background source galaxies must be identified in order to carry out lensing analysis. Galaxies in the CFHTLS-Deep catalogue were considered 'background' only if they were separated from the lens galaxy by $\Delta z \equiv z_S - z_L \geq 0.4$, where z_s is the redshift of the background source. The larger the value of Δz, the more likely it is that a source is actually located behind the lens. However, as Δz increases, the number of lens-source pairs decreases, thereby diminishing the weak galaxy-galaxy lensing signal. With the CFHTLS-Deep data, a large separation in redshift space was necessary in order to account for the uncertainties in photometric redshifts. The value of $\Delta z = 0.4$ was found to be an appropriate cut for the dataset; one that clearly separated background from foreground galaxies, while maintaining a source density of $\sim$15 galaxies per square arcminute.

Additionally, we impose a cut in angular separation when identifying background source galaxies. We only consider the gravitational lensing of a background galaxy by a foreground galaxy if they are separated by less than $\theta_{max} = 2'$. Although in principle every background galaxy will be lensed by every foreground galaxy, in practice the distortion becomes too weak to detect beyond θ_{max}. For lens galaxies in the field, this is because at $\theta \sim 2'$, the shear due to galaxy-galaxy lensing is on order with that due to large scale structure. For lens galaxies in group environment, the gravitational effects of the nearest galaxy neighbour will be felt at ~ 1 Mpc (which corresponds to

$\sim 2'$ at a redshift of $z = 0.05$) (Zehavi et al., 2005). Thus, it will not be possible to observationally detect dark matter halo truncation if it occurs at separations larger than ~ 1 Mpc. We therefore gain little by extending our analysis to lens-source galaxy pairs with separations larger than $2'$

We also reject all sources falling within an angular separation of $\theta_{min} = 5''$. Tyson et al. (1984) found that within this inner bound, the measurement of the source galaxy shape is contaminated by light from the lens (see also Brainerd et al., 1996; Kleinheinrich et al., 2006, though the latter impose a more conservative cut of $\theta_{min} = 8''$).

A summary of the CFHTLS-Deep dataset is given in Table 3.1, while a comparison of the redshift and magnitude distributions are shown in Figures 3.1 and 3.2. It is interesting that while there are more field lenses than group by over two orders of magnitude, there is only one order of magnitude more lens-source pairs (see Table 3.1). Comparing the redshift distributions, this difference can be attributed to the fact field galaxies are found at typically higher redshifts compared to the group galaxies. This means, compared to group galaxies, there are fewer source galaxies located behind field galaxies available for pair identification. Regardless, both the field and group samples are large enough to provide excellent weak galaxy-galaxy lensing statistics.

3.2 CNOC2 & GEEC

The second Canadian Network for Observational Cosmology[3] (CNOC2) Redshift Survey conducted (U, B, V, R_c, I_c)-band imaging in four patches,

[3] http://www.astro.utoronto.ca/∼cnoc/cnoc2.html

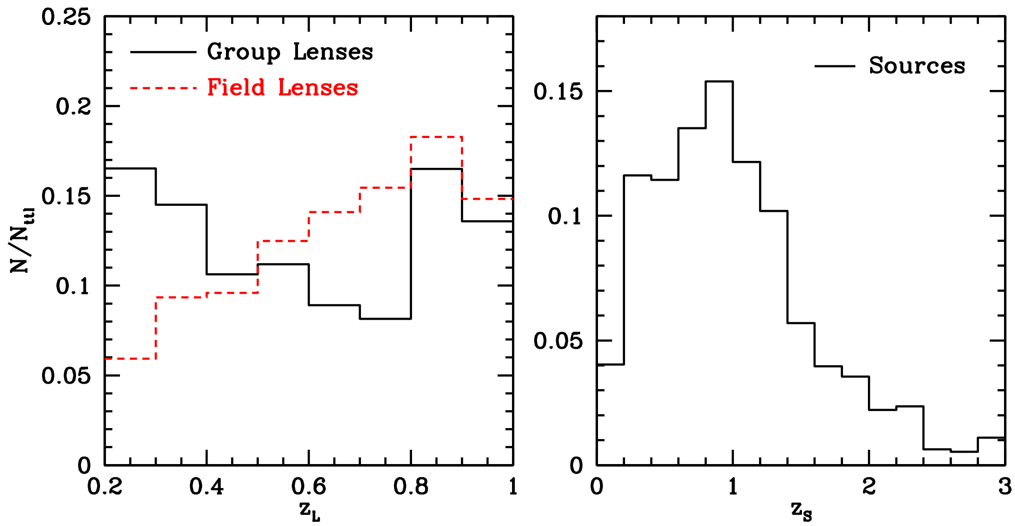

Figure 3.1: Redshift distribution of the CFHTLS-Deep lens (left panel) and source galaxies (right panel). As seen in the right panel, the field lens galaxies (dashed red) are found at systematically higher redshifts compared to the group lens galaxies (solid black).

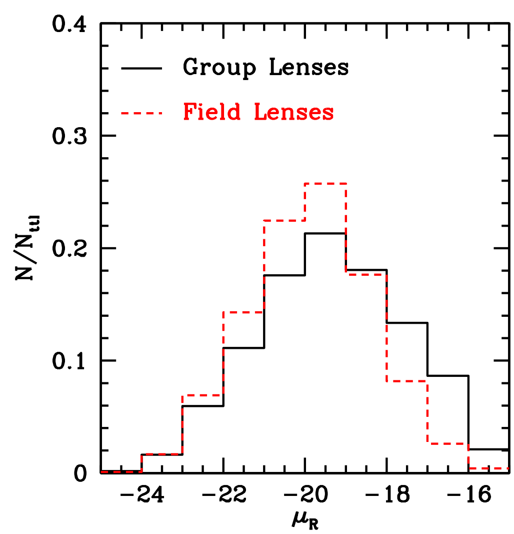

Figure 3.2: Absolute R-band magnitude distribution of the CFHTLS-Deep field (red dashed) and group (solid black) lens galaxies.

		Group Lenses			Field Lenses	
	N_S	N_{grps}	N_L	N_P	N_L	N_P
D1	103,776	29	1,237	180,842	51,232	7,478,392
D2	99,722	38	1,448	185,693	53,761	6,689,096
D3	121,321	78	2,887	580,659	47,782	7,627,925
D4	90,769	73	2,181	294,639	43,149	5,541,590
Total	415,588	218	7,753	1,241,833	195,524	27,337,003

Table 3.1: Information about the CFHTLS-Deep datasets divided by image field. From left to right, columns are: 1) image field, 2) number of sources N_S, 3) number of groups N_{grp}, 4) number of group galaxy lenses N_L, 5) number of lens-source pairs identified for the group galaxies N_P, 6) number of field galaxy lenses, and 7) number of lens-source pairs identified for the field galaxies.

totalling 1.5 degrees^2 in area. The survey obtained photometry for ~40,000 galaxies in the redshift range $0.1 < z < 0.6$ (Yee et al., 2000), and spectra of more than 6000 galaxies using the MOS spectrograph at the Canada-France-Hawaii Telescope (CFHT). Using these data, Carlberg et al. (2001) identified over 200 galaxy groups using a friends-of-friends algorithm (Huchra & Geller, 1982). The Group Environment and Evolution Collaboration (GEEC) have obtained extensive spectroscopic (Wilman et al., 2005), multi-wavelength photometric (Balogh et al., 2009), and X-ray (Finoguenov et al., 2009, Connelly et al., in prep) follow-up for these groups, allowing their properties to be studied in detail. In particular, the velocity dispersion of each group has been measured (Wilman et al., 2005). Owing to the spectroscopic data, the fraction of interlopers in these groups is extremely low (McGee et al., 2009).

For our weak galaxy-galaxy lensing analysis, we make use of two of the four CNOC2 fields (14 hr and 21 hr) where we have shape catalogues in hand. By combining these data with the GEEC group information, we have generated catalogues of group and field lens galaxies (Table 3.2). A comparison of redshift and magnitude distributions of the two catalogues are given in Figures 3.3 and 3.4. We have restricted lens galaxies to those with redshifts $0.1 \leq z_L \leq 0.544$ in order to ensure the field and group lens catalogues cover the same range.

A catalogue of source galaxies has likewise been generated using the CNOC2 data. The photometric redshifts of these galaxies have been measured using the Hyperz[4] code (Bolzonella et al., 2000),[5] and their shapes previously measured by Parker et al. (2005) (see also Finoguenov et al., 2009). As with the CFHTLS-Deep data sets, the contribution of a source galaxy to the weak galaxy-galaxy lensing signal is only considered if the source lays within $\theta_{max} = 2'$ and beyond $\theta_{min} = 5''$. The availability of spectroscopic redshifts for the lens galaxies means we need only impose a separation of $\Delta z \approx 0.1$ between lens and source galaxy in redshift space. The actual separation used depends on the uncertainty in the photometric redshift of the source; if the uncertainty in the source redshift is σ_z, we require $\Delta z \equiv z_S - z_L > \sigma_z$. As with the CFHTLS-Deep datasets, the density of sources behind our CNOC2 lens galaxies is ~ 15 arcmin^{-2}. A summary of the CNOC2 field and GEEC group lens galaxy datasets is given in Table 3.2.

A brief comparison of the CFHTLS-Deep and CNOC2/GEEC datasets is given in Table 3.3.

[4] http://webast.ast.obs-mip.fr/hyperz/

[5] See Russel Blackport's undergraduate thesis for details.

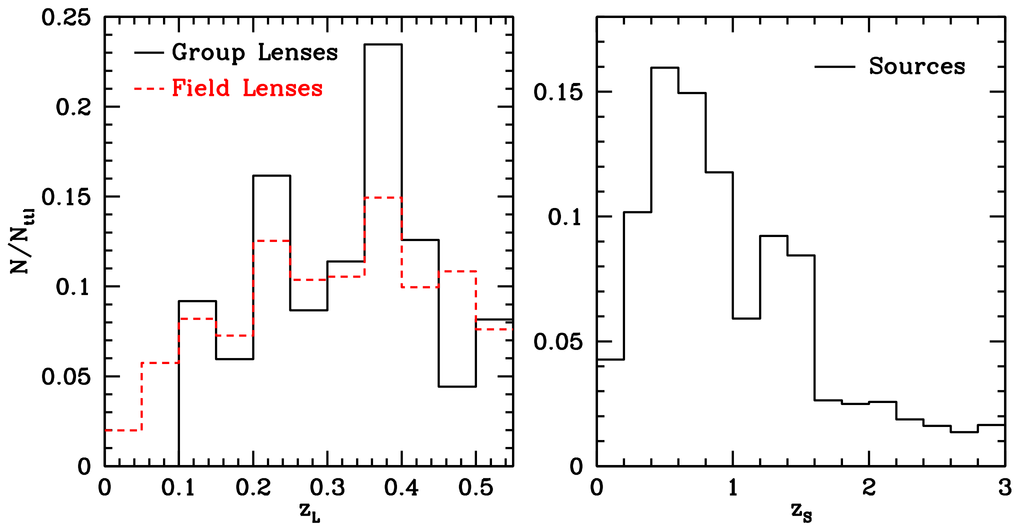

Figure 3.3: Redshift distribution of the CNOC2 lens (left panel) and source galaxies (right panel). As seen in the right panel, the CNOC2 field lens galaxies (dashed red) are found at lower redshifts than the GEEC group lens galaxies (solid black). The redshifts of both group and field galaxies are therefore restricted to $0.1 \leq z_L \leq 0.544$ for analysis.

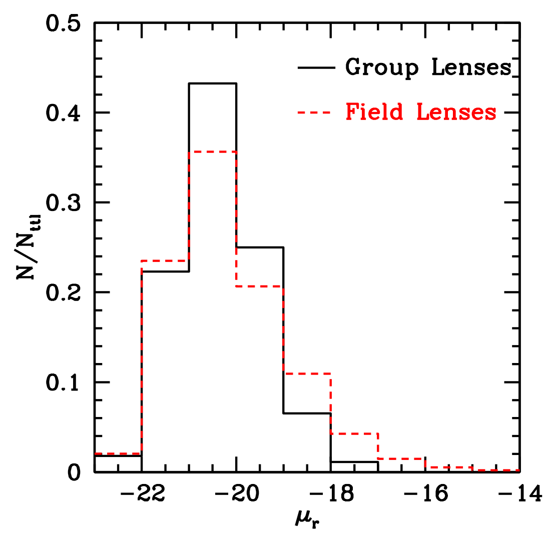

Figure 3.4: Absolute R_C-band magnitude distribution of the CNOC2 field (red dashed) and GEEC group (solid black) lens galaxies. The field galaxies are fainter on average; for the field galaxies, $\langle \mu_R \rangle = -19.56$, while for group galaxies $\langle \mu_R \rangle = -19.91$.

		Group Lenses				Field Lenses		
	N_S	N_{grp}	$N_{L,opt}$	$N_{L,x}$	N_P	$N_{L,opt}$	$N_{L,x}$	N_P
14 hour	23,612	40	347	3	48,370	1,051	76	137,565
21 hour	19,739	40	373	21	99,775	1,001	52	99,775
Total	43,351	80	720	24	86,721	2,052	128	237,340

Table 3.2: Information about the CNOC2 field and GEEC group lens galaxy datasets divided by image field. From left to right, columns are: 1) image field, 2) number of sources N_S in that field, 3) number of groups N_{grp}, 4) number of group galaxy lenses identified optically $N_{L,opt}$, 5) number of group galaxy lenses identified with x-rays $N_{L,x}$, 6) number of lens-source pairs identified for the group galaxies N_P, 7) number of field galaxy lenses identified optically, 8) number of field galaxy lenses identified with x-rays, and 9) number of lens-source pairs identified for the field galaxies.

	N_P	$\langle \mu_R \rangle$	$\langle z_L \rangle$	$\langle z_S \rangle$	$\langle M_\star \rangle$
CFHTLS-Deep:					
Field Lenses	27,337,003	-19.55	0.58	1.58	–
Group Lenses	1,242,833	-18.94	0.47	1.50	–
CNOC2 & GEEC:					
Field Lenses	237,340	-19.57	0.34	1.24	9.04×10^9
Group Lenses	86,721	-19.91	0.34	1.21	1.76×10^{10}

Table 3.3: A brief comparison of the CFHTLS-Deep and CNOC2/GEEC datasets, separated by lens type. From left to right, columns are: 1) lens type, 2) number of pairs N_P, 3) weighted mean magnitude, $\langle \mu_R \rangle$, of lens galaxies in the lens-source pairs catalogue, 4) weighted mean lens redshift $\langle z_L \rangle$, 5) weighted mean source redshift $\langle z_s \rangle$, and 6) weighted mean stellar mass $\langle M_\star \rangle$.

Bibliography

Anderson, R. 2009, Searching for Galaxy Groups in Photometric Data from the CFHT Legacy Survey (McMaster University Master's Thesis)

Balogh, M. L., McGee, S. L., Wilman, D., Bower, R. G., Hau, G., Morris, S. L., Mulchaey, J. S., Oemler, Jr., A., Parker, L., & Gwyn, S. 2009, MNRAS, 398, 754

Bolzonella, M., Miralles, J.-M., & Pelló, R. 2000, A&A, 363, 476

Brainerd, T. G., Blandford, R. D., & Smail, I. 1996, ApJ, 466, 623

Carlberg, R. G., Yee, H. K. C., Morris, S. L., Lin, H., Hall, P. B., Patton, D. R., Sawicki, M., & Shepherd, C. W. 2001, ApJ, 552, 427

Finoguenov, A., Connelly, J. L., Parker, L. C., Wilman, D. J., Mulchaey, J. S., Saglia, R. P., Balogh, M. L., Bower, R. G., & McGee, S. L. 2009, ApJ, 704, 564

Hoekstra, H., Franx, M., Kuijken, K., & Squires, G. 1998, ApJ, 504, 636

Huchra, J. P. & Geller, M. J. 1982, ApJ, 257, 423

Ilbert, O., Arnouts, S., McCracken, H. J., Bolzonella, M., Bertin, E., Le Fèvre, O., Mellier, Y., Zamorani, G., Pellò, R., Iovino, A., Tresse, L., Le Brun, V., Bottini, D., Garilli, B., Maccagni, D., Picat, J. P., Scaramella, R., Scodeggio, M., Vettolani, G., Zanichelli, A., Adami, C., Bardelli, S., Cappi, A., Charlot, S., Ciliegi, P., Contini, T., Cucciati, O., Foucaud, S., Franzetti, P., Gavignaud, I., Guzzo, L., Marano, B., Marinoni, C., Mazure, A., Meneux, B., Merighi, R., Paltani, S., Pollo, A., Pozzetti, L., Radovich, M., Zucca, E., Bondi, M., Bongiorno, A., Busarello, G., de La Torre, S., Gregorini, L., Lamareille, F., Mathez, G., Merluzzi, P., Ripepi, V., Rizzo, D., & Vergani, D. 2006, A&A, 457, 841

Kaiser, N., Squires, G., & Broadhurst, T. 1995, ApJ, 449, 460

Kleinheinrich, M., Schneider, P., Rix, H.-W., Erben, T., Wolf, C., Schirmer, M., Meisenheimer, K., Borch, A., Dye, S., Kovacs, Z., & Wisotzki, L. 2006, A&A, 455, 441

Li, I. H. & Yee, H. K. C. 2008, AJ, 135, 809

McGee, S. L., Balogh, M. L., Bower, R. G., Font, A. S., & McCarthy, I. G. 2009, MNRAS, 400, 937

Parker, L. C., Hudson, M. J., Carlberg, R. G., & Hoekstra, H. 2005, ApJ, 634, 806

Springel, V., White, S. D. M., Jenkins, A., Frenk, C. S., Yoshida, N., Gao, L., Navarro, J., Thacker, R., Croton, D., Helly, J., Peacock, J. A., Cole, S., Thomas, P., Couchman, H., Evrard, A., Colberg, J., & Pearce, F. 2005, Nature, 435, 629

Tyson, J. A., Valdes, F., Jarvis, J. F., & Mills, Jr., A. P. 1984, ApJ, 281, L59

Wilman, D. J., Balogh, M. L., Bower, R. G., Mulchaey, J. S., Oemler, A., Carlberg, R. G., Morris, S. L., & Whitaker, R. J. 2005, MNRAS, 358, 71

Yee, H. K. C., Morris, S. L., Lin, H., Carlberg, R. G., Hall, P. B., Sawicki, M., Patton, D. R., Wirth, G. D., Ellingson, E., & Shepherd, C. W. 2000, ApJS, 129, 475

Zehavi, I., Zheng, Z., Weinberg, D. H., Frieman, J. A., Berlind, A. A., Blanton, M. R., Scoccimarro, R., Sheth, R. K., Strauss, M. A., Kayo, I., Suto, Y., Fukugita, M., Nakamura, O., Bahcall, N. A., Brinkmann, J., Gunn, J. E., Hennessy, G. S., Ivezić, Ž., Knapp, G. R., Loveday, J., Meiksin, A., Schlegel, D. J., Schneider, D. P., Szapudi, I., Tegmark, M., Vogeley, M. S., & York, D. G. 2005, ApJ, 630, 1

Chapter 4

CFHTLS-Deep Results

As stated, the CFHTLS-Deep data cannot be used for detailed comparison of group and field halo properties owing to the uncertainties associated with photometric redshifts. In addition, the CFHTLS-Deep groups do not have group velocity dispersions or stellar masses. They therefore cannot be used to investigate the distribution of dark matter within groups nor measure dark matter-to-stellar mass ratios. However, the immense size of the datasets make them ideal for testing the basic stacking method and maximum likelihood technique.

4.1 Entire Sample

4.1.1 Basic Stacking Results

Tangential shear profiles for the CFHTLS-Deep group and field lens galaxy samples are shown in Figure 4.1. The magnitude of tangential shear in these plots, $\gamma_t \lesssim 0.007$, is consistent with that found by Jennifer Golding's analysis of the same CFHTLS-Deep data with no group/field classification (Golding, 2009). Fitting a singular isothermal sphere to these data gives best-fit velocity dispersions of $\sigma = 87 \pm 7$ km s^{-1} for the field galaxies, and $\sigma = 87 \pm 28$ km s^{-1} for the group galaxies. These values agree within error with Golding (2009), who find $\sigma = 85 \pm 7$ km s^{-1}. When scaled to the luminosity of an L^* galaxy, we find the velocity dispersion of group and field galaxies are $\sigma_* = 106 \pm 9$ km s^{-1} and $\sigma_* = 123 \pm 40$ km s^{-1}, respectively. This indicates that within error, group and field galaxies are best fit by dark matter haloes of the same mass. Results have been summarized in Table 4.1.

Visually, the field galaxies in Figure 4.1 appear to be well represented by a singular isothermal sphere mass model. The group galaxy data is noisey, and therefore does not. We can remove some of this noise by restricting our analysis to only the brightest group galaxies (with $\mu_R \leq -20$), thereby eliminating the majority of low mass galaxies. Since low mass lens galaxies induce only small amounts on tangential shear in background source galaxies, they suppress the tangential shear signal plotted in Figure 4.1, particularly in the innermost bins. As shown in Figure 4.2, the brightest CFHTLS-Deep group galaxies appear to be better fit by an isothermal sphere model, though the lens sample is small so the error bars are large.

It is possible to confirm that the observed tangential shear signal is real by measuring cross shear, γ_x. Cross shear is obtained by rotating source galaxy shapes by 45° before performing the basic stacking analysis (Wilson et al., 2001). Since gravitational lensing will causes images of source galaxies to be stretched tangential to the lens galaxy, rotating the source galaxy shapes in this way should cause the gravitational lensing signal to vanish. As shown

	N_P	**Basic Stacking** σ_* (km s^{-1})	**Maximum Likelihood** σ_* (km s^{-1})	s_* (kpc)
Field Lenses				
$\theta_{max} = 2'$	27,328,934	106 ± 9	169 ± 3	42 ± 3
low-z & bright	3,730,608	98 ± 8	148^{+5}_{-7}	48^{+11}_{-5}
low-z & faint	10,941,292	113 ± 8	133 ± 3	≥ 300
high-z & bright	6,877,678	97 ± 9	160^{+7}_{-11}	54^{+9}_{-3}
high-z & faint	5,779,356	76 ± 32	163 ± 21	72^{+39}_{-21}
Group Lenses				
$\theta_{max} = 2'$	1,241,347	123 ± 40	139^{+3}_{-9}	≥ 252
low-z & bright	178,807	98 ± 23	109^{+6}_{-12}	≥ 168
L^*-scaling off	”	119 ± 27	127^{+12}_{-18}	≥ 240
$\eta = 3$	”	92 ± 21	97^{+6}_{-6}	≥ 156
1/3 N_P	57,161	114 ± 40	139^{+18}_{-24}	≥ 72
low-z & faint	722,463	95 ± 90	223^{+15}_{-9}	≥ 244
high-z & bright	180,497	108 ± 41	–	–
high-z & faint	158,560	179 ± 67	290^{+75}_{-55}	≥ 90

Table 4.1: The effect of various data cuts and parameter selections on basic stacking and maximum likelihood results. N_P is the number of lens-source pairs, and θ_{max} the maximum angular separation applied when defining lens-source pairs (see Chapter 3). Lens galaxies are classified as low-z if $z_L \leq 0.6$, high-z if $z_L > 0.6$, bright if $\mu_R \leq -20$ and faint if $\mu_R > -20$. For the high-z & bright sample of group galaxies, maximum likelihood analysis was could constrain neither velocity dispersion nor truncation radius.

in the lower panels of Figure 4.1, the cross shear profiles for the CFHTLS-Deep field and group lenses are consistent with zero. This indicates that the observed tangential shear profiles are real, and caused by gravitational lensing.

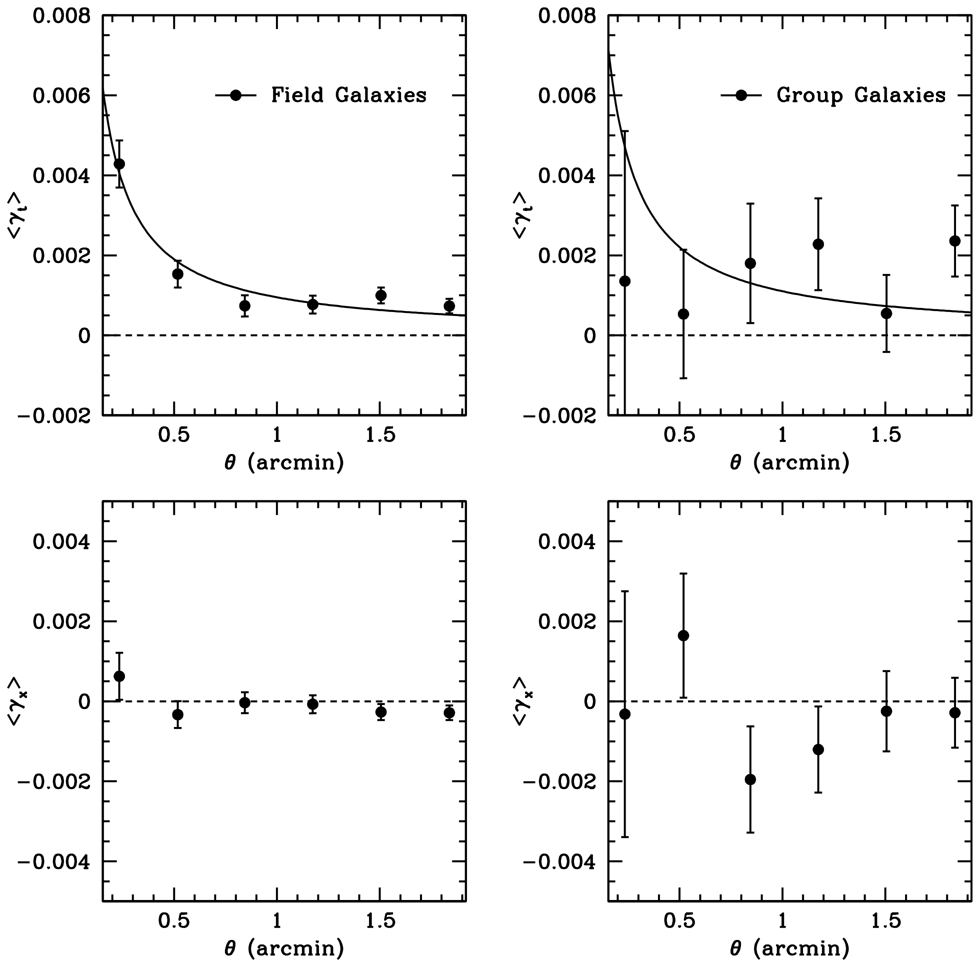

Figure 4.1: (Upper panels) Tangential shear profiles obtained for the entire sample of CFHTLS-Deep field (upper left) and group (upper right) lens galaxies. The solid line shows the best fitting singular isothermal sphere density profile, while the dashed line is for reference. (Lower panels) Cross shear profiles obtained by rotating galaxy shapes by 45°. The cross shear profiles obtained for both the field (lower left) and group (lower right) lens galaxies are consistent with zero, indicating the observed tangential shear profiles are due to gravitational lensing. Note the different scales between the upper and lower panels.

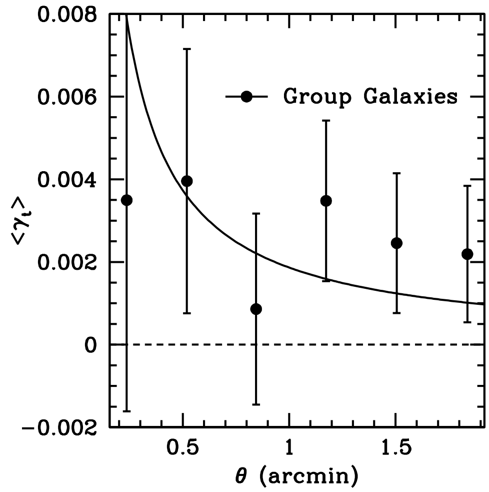

Figure 4.2: Tangential shear profile obtained for the brightest ($\mu_R \leq -20$) CFHTLS-Deep group galaxies. The solid line shows the singular isothermal sphere of best-fit. Compared to the tangential shear profile of the entire group sample (upper right panel of Figure 4.1), the bright group galaxies appear to better follow a singular isothermal trend.

4.1.2 Maximum Likelihood Results

Results from maximum likelihood analysis of the CFHTLS-Deep field and group galaxies are shown in Figure 4.3. While velocity dispersion σ_* could be constrained for both samples (169 ± 3 km s^{-1} for field galaxies and 139^{+3}_{-9} km s^{-1} for group), truncation radius s_* could only be constrained for the field galaxies (42 ± 3 kpc). For the group sample, σ_* agrees with results from the basic stacking method (see Table 4.1). For the field sample, however, σ_* was large compared to results from the basic stacking analysis, and s_* low compared to results from, for example, Hoekstra et al. (2004). Such authors find the radial extents of field galaxies to be $\gtrsim 150$ kpc. Within error, we expect the maximum likelihood and basic stacking analyses to agree. In an attempt to understand this discrepancy - and perhaps identify a subset of data which constrains group galaxy truncation radius - the data has been divided into subsamples based on lens magnitude and redshift.

As with the basic stacking method, the maximum likelihood technique can be used to determine test whether the gravitational lensing signal is real. Again, this is done by rotating source shapes by 45° and repeating analysis. As shown in the lower panels of Figure 4.3, the rotated sources yield (σ_*, s)-pairs that correspond to dark matter haloes of zero mass. Hence, the maximum likelihood contours are real.

4.2 Data Cuts

To generate subsamples, lens galaxies were classified according to their redshift and absolute R_C-band magnitude. A lens galaxy is classified as low redshift if $z_L \leq 0.6$ and high redshift if $z_L > 0.6$. Bright lens galaxies are defined as those with $\mu_R \leq -20$, and faint with $\mu_R > -20$. Lens galaxies are then divided into four subsamples: low-z & bright, low-z & faint, high-z & bright, and high-z & faint. Basic stacking and maximum likelihood analysis were then repeated on these four subsamples.

The best-fit σ_*-values for the basic stacking method are recorded in Table 4.1 for both the CFHTLS-Deep field and group lens galaxies. Maximum likelihood contours of all subsamples are plotted (Figure 4.4) as well as tabulated (Table 4.1). What should be taken away from these results is that, for the group galaxies, it does not appear possible to constrain s_*. Although this is not encouraging, it is also not surprising. Truncation radius is notoriously a very hard parameter to constrain using weak galaxy-galaxy lensing (see, for e.g., Schneider & Rix, 1997; Hudson et al., 1998).

In all group galaxy subsamples, the best-fit σ_*-values obtained from the maximum likelihood contours agree with those from the basic stacking analysis. This is not true of the field galaxies, for which the maximum likelihood and basic stacking velocity dispersions never agree. This is something that needs to be understood.

4.3 Testing

To ensure the code is functioning as expected, and to test the role of chosen parameters, basic stacking and maximum likelihood analysis were conducted following a series of data cuts and parameter variations.

4.3.1 Decreasing the Number of Pairs

If the basic stacking and maximum likelihood methods are functioning properly, we expect that decreasing the number of pairs should increase the uncertainties in best fit values, though the best fit values should agree within error. As shown in Figure 4.5, this is indeed the case. Where as $\sigma_* = 109^{+6}_{-12}$ for the entire sample of low-z, bright group lenses (i.e., with $z_L \leq 0.6$ and $\mu_R \leq -20$), reducing the number of pairs by a factor of ~ 3 gives $\sigma_* = 139^{+18}_{-24}$. These two values agree within error. All values are summarized in Table 4.1.

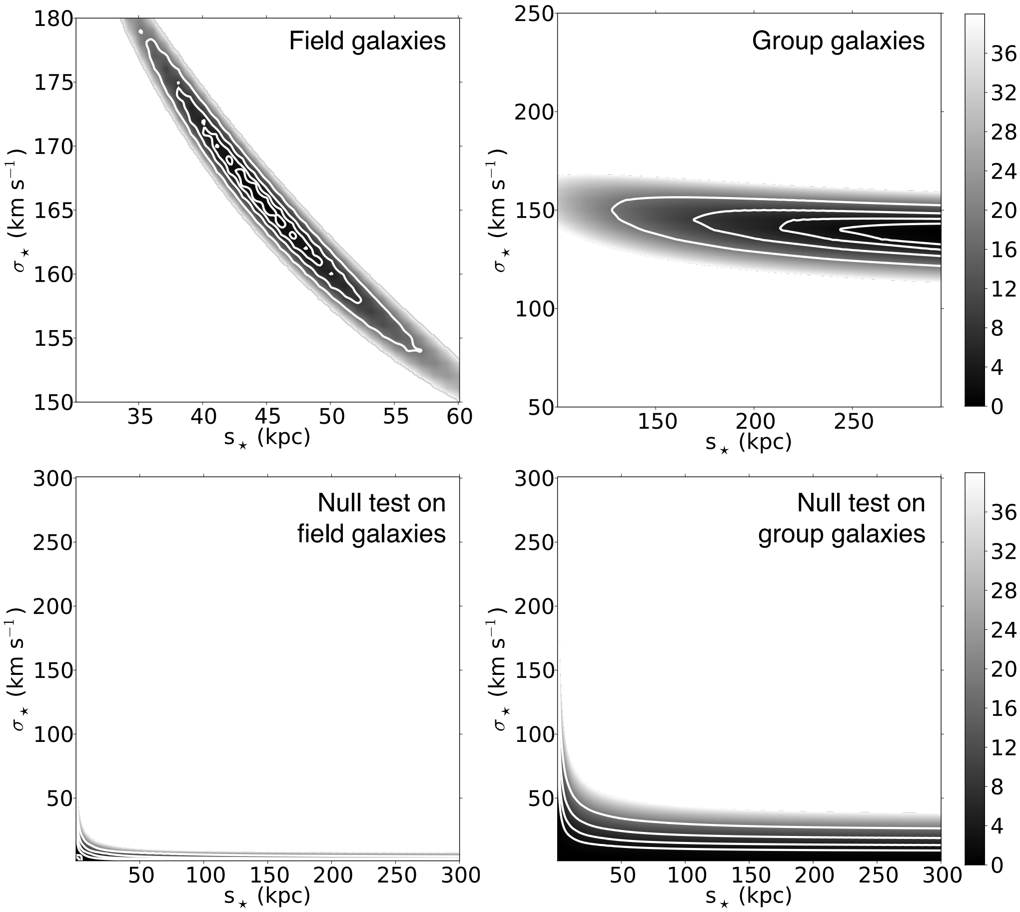

Figure 4.3: (Upper panels) Maximum likelihood contours obtained for the entire sample of CFHTLS-Deep field (upper left) and group (upper right) lens galaxies. As in Figure 2.6, contours represent the 1-σ, 2-σ, 3-σ and 4-σ levels of confidence in the best fitting mass model. (Lower panels) The maximum likelihood technique can be tested by rotating galaxy shapes by 45°, in analogy with cross shear. The (σ_*, s_*)-pairs traced by these null contours give rise to zero tangential shear for both the field (lower left) and group (lower right) lens galaxies, indicating that the contours in the upper panels are real. Note that the non-smooth nature of the 1-σ contours is an artifact of resolution of the code.

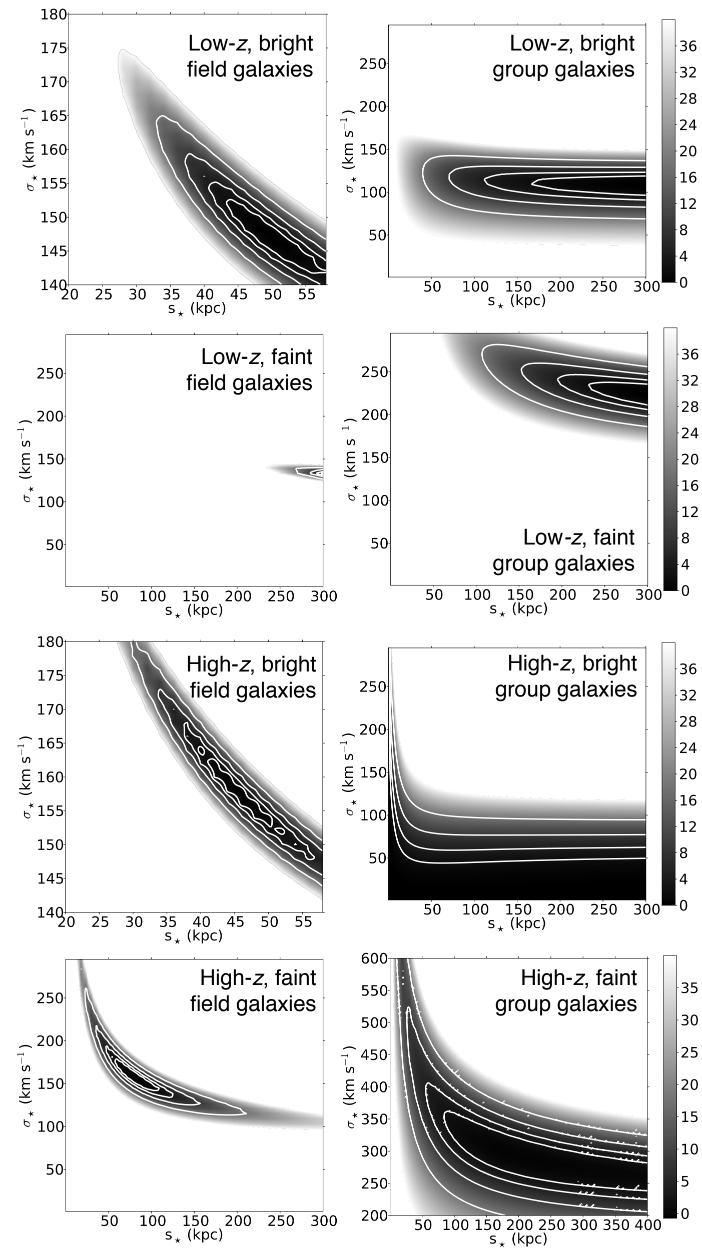

Figure 4.4: Maximum likelihood contours for various magnitude and redshift cuts of the CFHTLS-Deep field (left panels) and group (right panels) lens galaxies. Subsamples are defined according to lens redshift and magnitude; low-z & bright ($z_L \leq 0.6$, $\mu_R \leq -20$; first row), low-z & faint ($z_L \leq 0.6$, $\mu_R > -20$; second row), high-z & bright ($z_L > 0.6$, $\mu_R \leq -20$; third row), high-z & faint ($z_L > 0.6$, $\mu_R > -20$; fourth row). As before, contours represent the 1-, 2-, 3- and 4-σ confidence intervals. Non-uniform contour lines are an artifact from the resolution of the maximum likelihood analysis.

4.3.2 Removing Luminosity Scaling

The average absolute R-band magnitude of the low-z & bright group sample is $\mu_R = -21.26$ at a redshift of $z = 0.4$. This is brighter than the absolute magnitude adopted for an L^*-galaxy (recall from Section 2.3.1, $\mu_R^* = -20.42$ at $z = 0.4$). We therefore expect $\sigma > \sigma_*$ and $s > s_*$. If we remove luminosity scaling from our analysis, we find this is true for both the basic stacking and maximum likelihood analysis (see Table 4.1). However, the change in best-fit parameters is small. With and without L^*-scaling, the best-fit parameters agree within error.

For reference, the effect of luminosity scaling on maximum likelihood contours has been illustrated in Figure 4.5. When luminosity scaling is excluded, contours become wider indicating an increase in uncertainty.

4.3.3 Varying η

To test the importance of the luminosity-scaling index, the adopted value of η was varied. Figure 4.5 illustrates the effect of changing η from 4 to 3. Since $\sigma/\sigma = (L/L_*)^{1/\eta}$, we expect this variation to decrease the best-fit values of σ_* and s_*. From Table 4.1, this is indeed observed, though the parameters obtained with $\eta = 3$ and $\eta = 4$ agree within error. Figure 4.5 also illustrates the fact that setting $\eta = 3$ marginally tightens the maximum likelihood contours of the low-z, bright CFHTLS-Deep group galaxies.

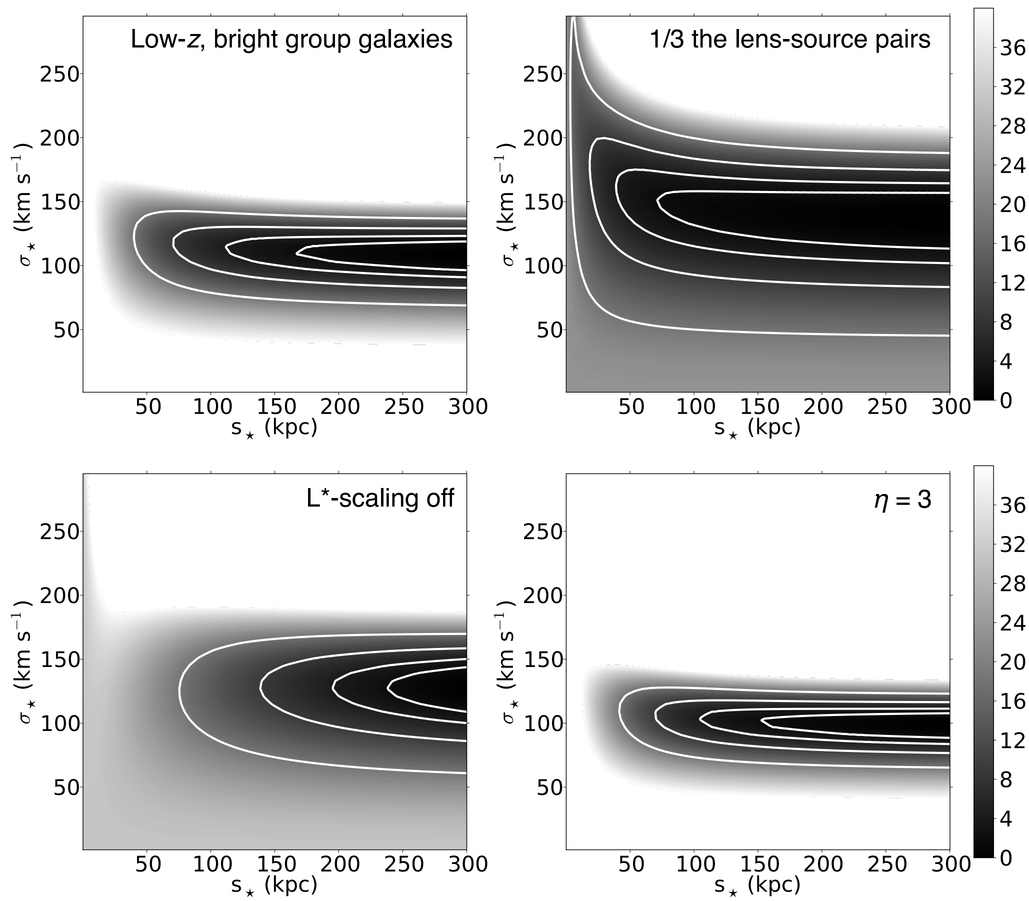

Figure 4.5: The effect of various parameters on maximum likelihood contours. (Upper left panel) The contours obtained for the entire sample of low-z ($z_L \leq 0.6$), bright ($\mu_R \leq -20$) CFHTLS-Deep group galaxies (see Table 4.1 for values of σ_* and s_*). Restricting analysis to approximately 1/3 the number of lens-source pairs (upper right) widens the contours, but the values of agree within error. (Lower left) Turning the L^*-scaling off, so that the dark matter halo of a lens galaxy is no longer scaled to that of an L^* galaxy, marginally increases the values of σ and s. (Lower right) Varying the luminosity-scaling index η appears to have no effect on the maximum likelihood contours.

Bibliography

Golding, J. 2009, Properties of Galaxy Dark Matter Halos using galaxy-galaxy weak lensing in the CFHTLS-Deep (McMaster University Master's Thesis)

Hoekstra, H., Yee, H. K. C., & Gladders, M. D. 2004, ApJ, 606, 67

Hudson, M. J., Gwyn, S. D. J., Dahle, H., & Kaiser, N. 1998, ApJ, 503, 531

Schneider, P. & Rix, H.-W. 1997, ApJ, 474, 25

Wilson, G., Kaiser, N., Luppino, G. A., & Cowie, L. L. 2001, ApJ, 555, 572

Chapter 5

GEEC Results

In this Chapter, results for the spectroscopic samples of CNOC2 field and GEEC group lens galaxies are presented. We first address the question of whether dark matter haloes are truncated in the group environment by comparing the best-fit halo parameters of the two data samples. We then examine how dark matter is distributed within groups themselves, and determine whether the halo-to-stellar mass ratio depends on environment.

5.1 Group and Field Dark Matter Haloes

5.1.1 Basic Stacking Results

Tangential shear profiles for the GEEC group and CNOC2 field lens galaxies are shown in Figure 5.1. From the basic stacking analysis, the field galaxies are found to be best fit by a dark matter halo with velocity dispersion $\sigma_* = 112 \pm 33$ km s^{-1} when luminosity scaling is included, and $\sigma = 93 \pm 27$ km s^{-1} when it is not. For the group galaxies, basic stacking analysis gives $\sigma_* = 214 \pm 35$ km s^{-1} and $\sigma = 190 \pm 31$ km s^{-1} (see also Table 5.1). This indicates that the average mass of a group galaxy in our sample is much greater than that of a field galaxy.

We have additionally conducted basic stacking analysis on only those lens galaxies with stellar masses. For these subsamples, we find the field and group galaxies are best-fit by dark matter haloes with $\sigma = 96 \pm 28$ km s^{-1} and $\sigma = 198 \pm 29$ km s^{-1}, respectively. These results are consistent with the values of obtained using the entire sample. As evident in Table 5.1, this is because restricting our analysis to only those galaxies with stellar masses decreases the number of lens-source pairs by $< 10\%$. In subsequent analysis, we will use these dark matter halo parameters to estimate the halo-to-stellar mass ratios of group and field galaxies.

It is important to note that our sample of field galaxies may be suffering from uncorrected systematics. Referring to Figure 5.1, we see that the cross shear profile is not consistent with zero. We hope to improve upon these systematics in the future through further investigation of the CNOC2 field galaxy catalogue.

5.1.2 Maximum Likelihood Results

The upper panels of Figure 5.2 show the maximum likelihood contours obtained for the entire sample of CNOC2 field and GEEC group galaxies. In agreement with basic stacking results, velocity dispersion is found to be $\sigma_* = 228^{+21}_{-15}$ km s^{-1} for the sample of group lenses (see Table 5.1). However, truncation radius is not constrained. It is possible to put a lower limit on the size of the GEEC group galaxy dark matter haloes; we find $s_* \geq 228$ kpc.

This possibly indicates that dark matter haloes are not truncated, and galaxies should be modelled with singular isothermal sphere profiles instead.

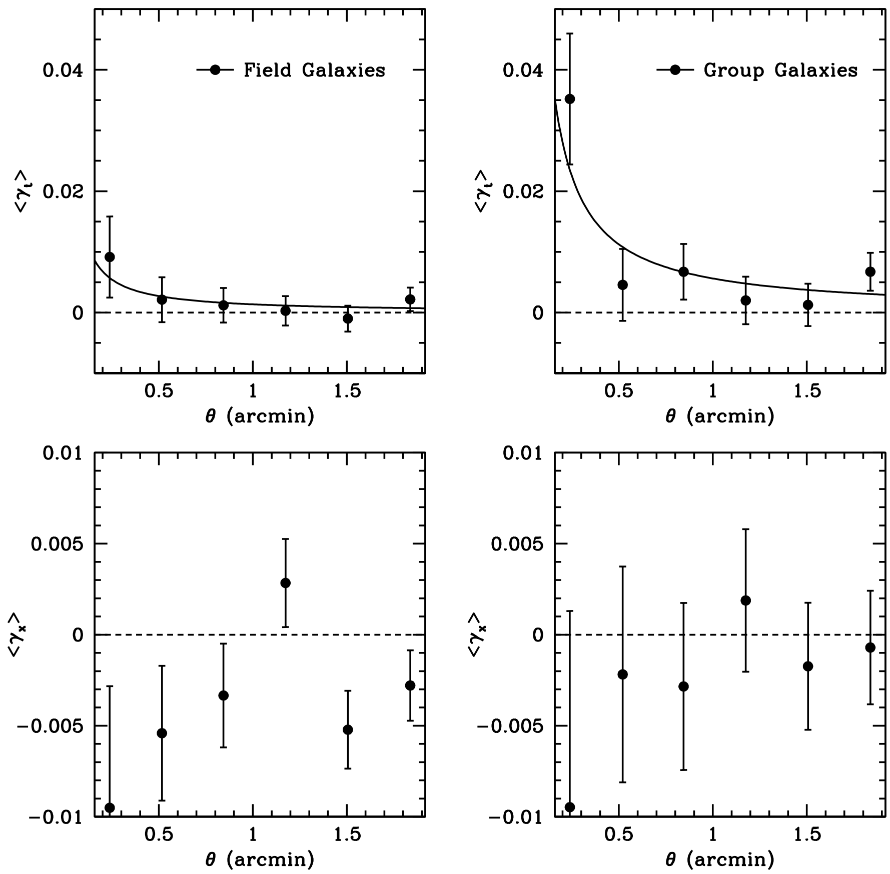

Figure 5.1: (Upper panels) Tangential shear profiles obtained for the entire sample of GEEC field (upper left) and group (upper right) lens galaxies. (Lower panels) Cross shear profiles obtained by rotating galaxy shapes by 90°. The cross shear profiles obtained for both the field (lower left) and group (lower right) lens galaxies are consistant with zero, indicating the observed tangential shear profile is due to gravitational lensing. Note the different scales between the upper and lower panels.

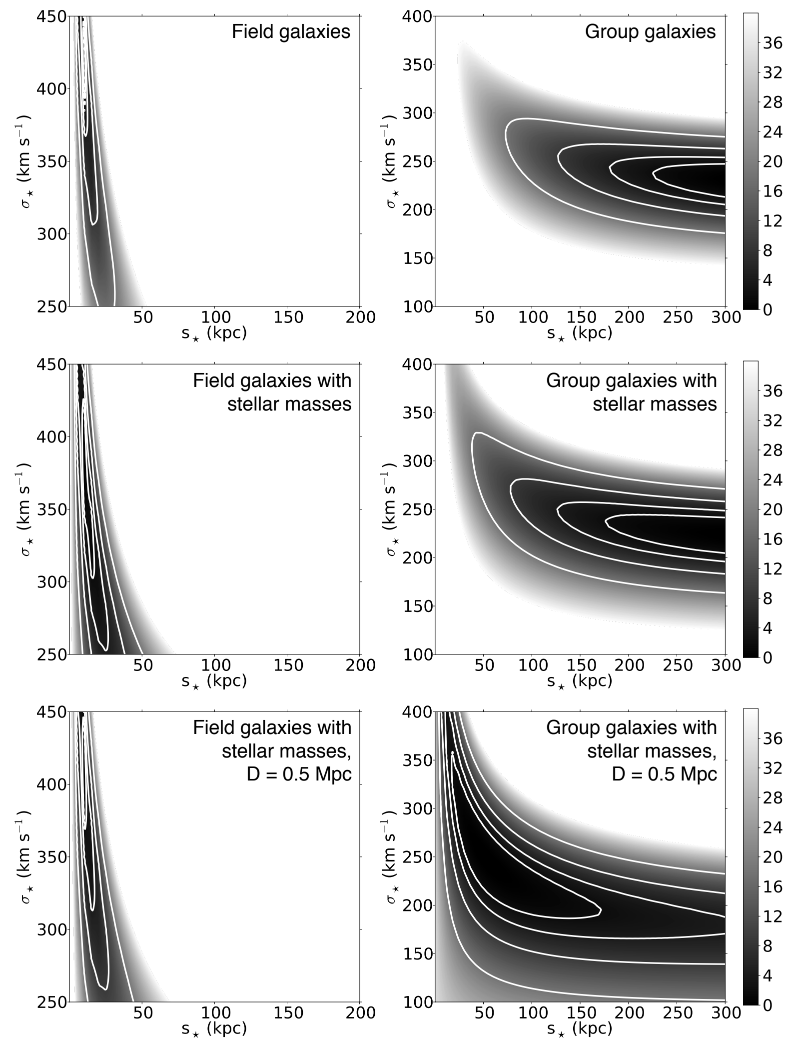

Figure 5.2: (Upper panels) Maximum likelihood contours obtained for the entire sample of GEEC field (upper left) and group (upper right) lens galaxies. Neither sample is constrained in both σ_* and s_*, and the field galaxies display un-physically high values of σ_*. (Middle panels) By limiting analysis to only those lens galaxies with stellar masses, contours are broadened slightly but agree within error. (Lower panels) Maximum likelihood contours obtained when lens-source pairs are considered if they fall within a physical separation of 0.5 Mpc, rather than an angular separation of 2 arcmin. The sample of GEEC group galaxies becomes constrained in both velocity dispersion and truncation radius, with $\sigma_* = 250^{+108}_{-60}$ km s^{-1} and $s_* = 54^{+117}_{-39}$ kpc. Note that not all sub-figures have the same range in σ_* and s_*.

Conversely, using the sample of field galaxies it is possible to constrain truncation radius but not velocity dispersion; we measure $\sigma_* \geq 254$ km s^{-1} and $s_* = 12^{+3}_{-9}$ kpc. This implies that the CNOC2 field galaxies have extremely massive, extremely truncated dark matter haloes. These results seem implausible, however, since the lower limit on σ_* is un-physical for a galaxy-sized dark matter halo. A velocity dispersion $\gtrsim 250$ km s^{-1} is comparable to that of a galaxy group or small galaxy cluster.

On possible explanation for these results are the residual systematics of the CNOC2 field galaxy shape catalogues. However, it is unlikely systematics alone can account for the un-physically large velocity dispersions. Either 1) there exist additional artifacts in the field galaxy data sample that are not being accounted for, or 2) a truncated isothermal sphere is the wrong adopted mass model for these data.

We suspect at least part of the solution lies with the data sample. Figure 5.3 illustrates how maximum likelihood contours of the CNOC2 field galaxies change when luminosity scaling is excluded. Both velocity dispersion and truncation radius become constrained in this instance, and the values of σ become more physical. The un-physical results thus seem to be linked to the luminosity scaling. This may be a result of bad galaxy magnitudes μ_R, or alternatively, the adopted value of μ_R^*.

On the other hand, the model may also be a factor. With both the CNOC2 and CFHTLS-Deep field galaxy samples, the best-fit σ_*-values from the maximum likelihood and basic stacking methods did not agree. The maximum likelihood technique traced mass models with large velocity dispersions. It is therefore possible that we do not understand the behaviour of our adopted mass model, and that it needs modifing or replacing. A more thorough investigation of both the CNOC2 field galaxies and adopted truncated isothermal sphere model is clearly is required.

The middle two panels of Figure 5.2 illustrate the effect of considering only those galaxies with stellar masses. Due the smaller number of lens-source pairs, uncertainty is increased slightly and the contours are widened. Within error, the results from these stellar mass-selected field and group samples agree with those from the entire data samples (Table 5.1).

Physical Separation

In order to determine if group galaxy dark matter haloes are truncated relative to field galaxies, we need to obtain constraints on σ_* and s_*. To this end, we investigate the effect of imposing a physical separation on lens source pairs as opposed to an angular separation. Rather than analyzing lens-source pairs with angular separations $\leq \theta_{max} = 2'$, pairs are considered if the physical separation between lens and source is $\leq D_{max} = 0.5$ Mpc (as measured in the lens galaxy plane). The value of D_{max} was chosen because at the mean lens galaxy redshift of $z_L \approx 0.3$, 0.5 Mpc corresponds to an angular separation of $\theta \approx 2'$. For lenses at low redshifts, selecting pairs based on physical as opposed to angular separation will increase the number of lens-source pairs. Conversly, for lenses at high redshifts, the number of pairs will decrease. As seen in Table 5.1, the overall effect of imposing a physical separation is to decreases the number of lens-source pairs slightly. Beyond 500 kpc, the distortion a foreground lens galaxy induces in a background source will be small. By eliminating these lens-source pairs from our analysis, we are effectively decreasing the noise.

The maximum likelihood contours obtained when imposing a physical separation are shown in the lower panels of Figure 5.2. Though the field sample remains unconstrained (and un-physically high) in σ_*, both velocity dispersion and truncation radius become constrained for the group sample. We find $\sigma_* = 250^{+108}_{-60}$ km s^{-1} and $s_* = 54^{+117}_{-39}$ kpc. The effect of imposing a physical separation on σ and s is also given in Table 5.1. Within error, these results agree with those obtained using angular separations. However, the σ of group galaxies decreases slightly.

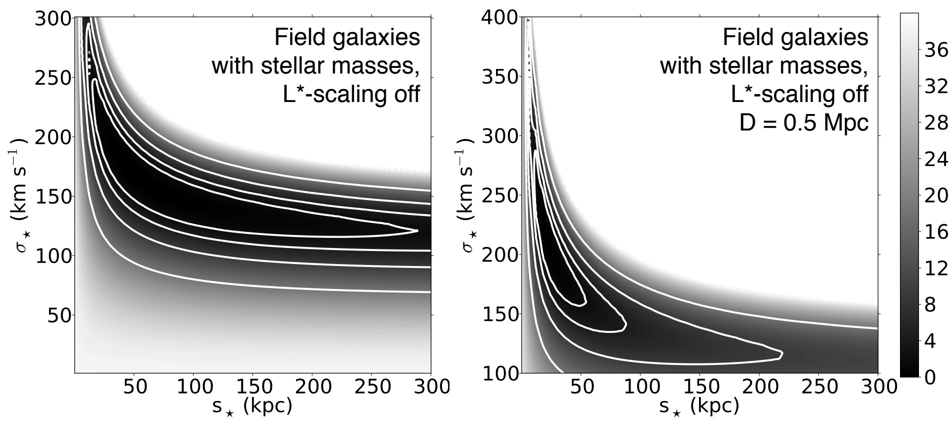

Figure 5.3: Maximum likelihood contours for the CNOC2 field galaxies when L^*-scaling is turned off. Both velocity dispersion σ and s are constrained. The two panels compare the contours obtained when (left panel) a angular separation of $\theta_{max} \leq 2'$ and (right) a physical separation of $D_{max} \leq 0.5$ Mpc are applied to lens-source pairs. In both panels, results plotted are for only those galaxies with stellar masses available. Note the different ranges of the left and right panels.

	N_P	**Basic Stacking** σ_* (km s^{-1})	**Maximum Likelihood** σ_* (km s^{-1})	s_* (kpc)
Field Lenses				
$\theta = 2'$	222,959	112 ± 33	≥ 254	12^{+3}_{-9}
L^*-scaling off	"	93 ± 27	360^{+33}_{-105}	6^{+9}_{-3}
with stellar masses:				
$\theta_{max} = 2'$	203,871	117 ± 34	≥ 300	10^{+8}_{-3}
L^*-scaling off	"	96 ± 28	169^{+105}_{-52}	48^{+243}_{-39}
$D_{max} = 0.5$ Mpc	202,849		≥ 370	8^{+5}_{-2}
L^*-scaling off	"		226^{+135}_{-69}	18^{+39}_{-15}
bright: $\mu_R \leq -19$	105,759		≥ 240	12^{+6}_{-3}
dim: $\mu_R \geq -20$	151,340		≥ 67	≥ 6
low-z: $z_l \leq 0.322$	134,872		≥ 270	12^{+15}_{-9}
high-z: $z_l > 0.322$	67,977		≥ 228	12^{+21}_{-3}
Group Lenses				
$\theta_{max} = 2'$	84,299	214 ± 35	232^{+15}_{-21}	≥ 228
L^*-scaling off	"	190 ± 31	216^{+27}_{-15}	≥ 150
with stellar masses:				
$\theta_{max} = 2'$	81,037	223 ± 33	226 ± 21	≥ 180
L^*-scaling off	"	198 ± 29	229^{+27}_{-30}	≥ 96
$D_{max} = 0.5$ Mpc	76,135		250^{+111}_{-63}	54^{+117}_{-39}
L^*-scaling off	"		214^{+45}_{-33}	72^{+52}_{-30}
weighting off	"		262^{+63}_{-45}	72^{+99}_{-39}
$\eta = 3$	"		244^{+141}_{-63}	48^{+123}_{-39}
Group halo subtracted	"		250^{+141}_{-69}	48^{+117}_{-39}

Table 5.1: The effect of various data cuts and parameter selections on basic stacking and maximum likelihood results. N_P is the number of lens-source pairs, and θ_{max} and D_{max} the maximum separations in angular and physical units, respectively applied when defining lens-source pairs.

Data Cuts

Various subsamples were identified within the CNOC2 field galaxy sample in order to determine if both σ_* and s_* could be constrained. Using a physical separation of 0.5 Mpc, maximum likelihood analysis was conducted on the bright ($\mu_R \leq -19$), faint ($\mu_R \geq -20$), low-z ($z_L \leq 0.322$) and high-z ($z_L > 0.322$) field galaxies separately. Results are shown in Figure 5.4 and values summarized in Table 5.1. For the bright, low-z and high-z subsamples, results are consistent with what was found for the entire data sample; only truncation radius is constrained and velocity dispersion values are extremely high. Using the faint subsample, neither σ_* nor s_* are constrained.

Testing

As with the CFHTLS-Deep data, the effect of various parameters on the GEEC group data was investigated to ensure the code was functioning. Figure 5.5 shows, in particular, the effect of removing the luminosity-scaling and changing the luminosity-scaling index η (see Section 4.3 for more details). Compared to the lower left panel in Figure 5.2, turning off L^*-scaling tightens the contours slightly. As was found for the CFHTLS-Deep data, varying η appears to have little effect on the maximum likelihood contours. In both cases, the values of σ_* and s_* agree with the contours shown in Figure 5.2.

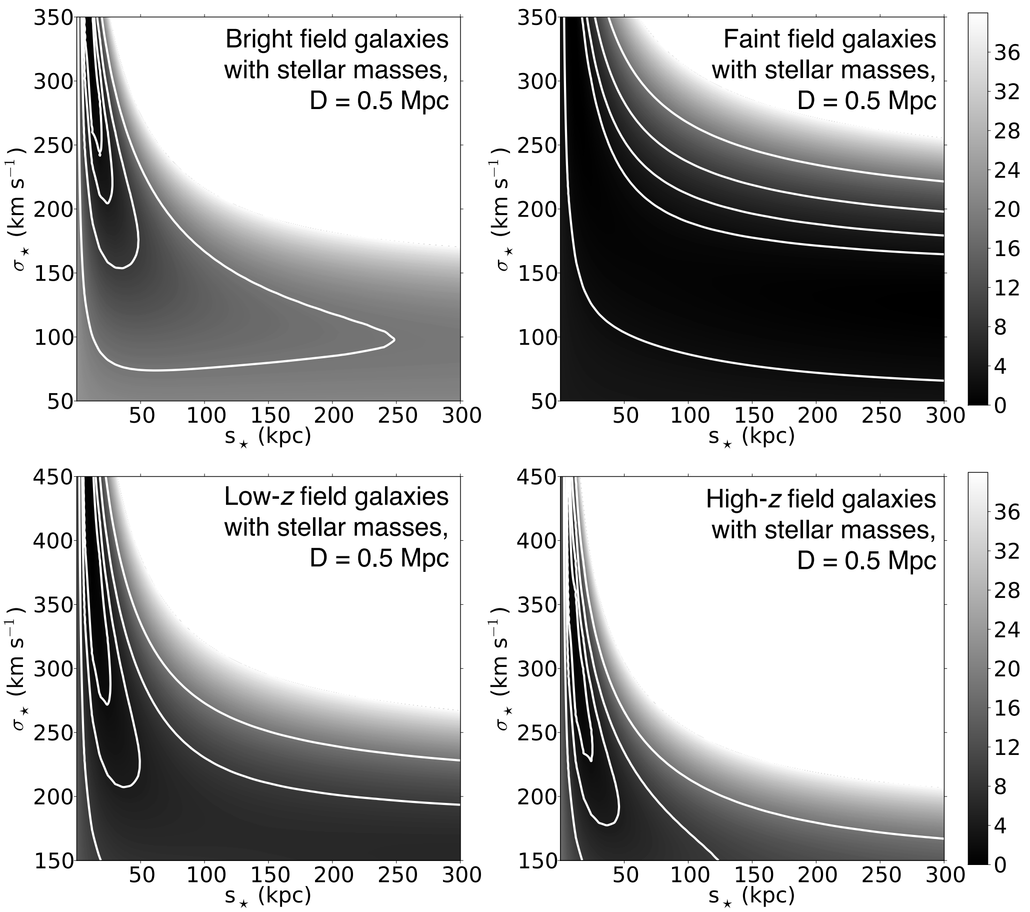

Figure 5.4: Maximum likelihood contours obtained for the brightest ($\mu_R \leq -19$; upper left), faintest ($\mu_R \geq -20$; upper right), nearest ($z_L \leq 0.322$; lower left) and furthest ($z_L > 0.322$; lower left) field galaxies. In all cases, analysis is limited to lens galaxies with stellar masses available and the maximum lens-source separation has been set as 0.5 Mpc. Note the difference in σ_*- and s_*-ranges between the upper and lower panels.

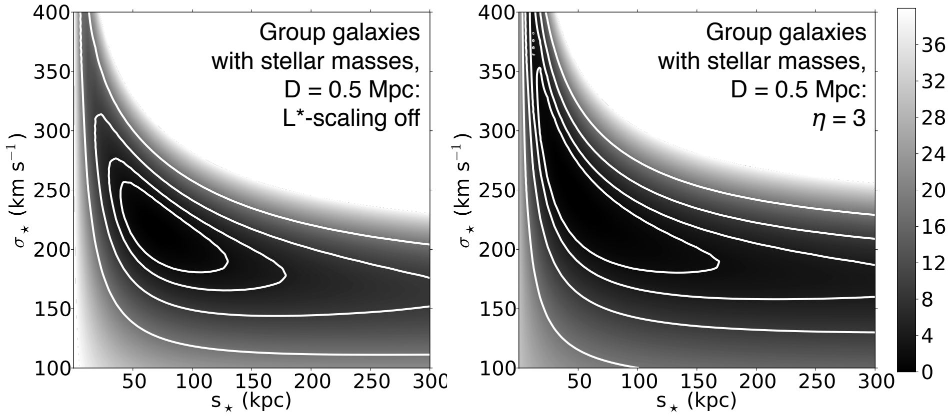

Figure 5.5: Maximum likelihood contours obtained for the sample of GEEC group lenses with stellar masses when lens-source maximum separation is $D = 0.5$ Mpc. The left panel shows the effect of removing L^*-scaling, and the right panel of setting $\eta = 3$.

5.1.3 Mean Tangential Shear

Since the maximum likelihood technique could not reliably constrain σ_* for the CNOC2 field galaxies, we make use of one additional method of quantifying dark matter haloes. This method is to simply calculate the mean tangential shear within some physical distance, D_{max}. We choose to set $D_{max} = 0.5$ Mpc, and calculate mean tangential shear according to equation (2.12):

$$\langle \gamma_t \rangle_{<0.5\ Mpc} = \frac{\sum_i e_{t,i} w_i}{\sum_i w_i},$$

where $e_{t,i}$ is the tangential shear measured for lens-source pair i, calculated as in the basic stacking method. The weighted mean separation $\langle \theta \rangle$ is similarly calculated. Velocity dispersion of the best fitting dark matter halo is then determined by assuming a singular isothermal sphere distribution (equtaion 2.14)

$$\langle\gamma_t\rangle_{<0.5\ Mpc} = \frac{\theta_e}{2\langle\theta\rangle} = \left(\frac{\sigma}{186\ \mathrm{km\ s^{-1}}}\right)^2 \frac{\beta}{2\langle\theta\rangle},$$

and the mass contained within $D_{max} = 0.5$ Mpc calculated as

$$M(<0.5\ \mathrm{Mpc}) = \frac{2\sigma^2\langle D\rangle}{G}.$$

Here, $\langle D\rangle$ is the mean lens-source separation in physical units.

The dark matter halo parameters obtained for the CNOC2 field and GEEC group lens galaxies are given in Table 5.2. In both cases, calculations were only carried out on those galaxies with stellar masses available. Since we will be comparing the halo-to-stellar mass ratios of group and field galaxies, the masses recorded in Table 5.2 have not been scaled according to an L^* galaxy; they have been calculated using σ rather than σ_*. As expected, the values of σ and σ_* are consistent with those determined using the basic stacking method.

	Field Lenses	**Group Lenses**
N_P	170,091	63,907
$\langle\gamma_t\rangle_{<0.5\ Mpc}$	0.0009 ± 0.0010	0.0046 ± 0.0020
$\langle\theta\rangle$ ($''$)	72.02 ± 0.07	71.7 ± 0.1
$\langle z_L\rangle$	0.3	0.3
σ (km s^{-1})	81 ± 55	185 ± 40
σ_* (km s^{-1})	102 ± 69	214 ± 46
$M(<0.5$ Mpc) ($M_\odot$)	2.42×10^{12}	1.06×10^{13}

Table 5.2: Total mean tangential shear of the GEEC group and CNOC2 field galaxies measured within 0.5 Mpc, and the resulting dark matter halo masses. Parameters used for the calculation are also given.

5.2 Smooth Halo Contribution

In order to determine how dark matter is distributed within galaxy groups, maximum likelihood analysis of the GEEC group galaxies (within $D_{max} = 0.5$ Mpc) was repeated with the tangential shear due to the smooth group halo accounted for. As described in Section 2.3.3, this was done by modelling the smooth group halo as a singular isothermal sphere. The amount of tangential shear induced by the group halo depends on two parameters; the velocity dispersion of the group and the distance to the group centre. The velocity dispersions used for this analysis were previously determined using line-of-sight velocities of member galaxies (Wilman et al., 2005). For reference, the average group velocity dispersion was $\sim$ 370 km s^{-1} for the GEEC groups analyzed here.

Figure 5.6 compares the contours obtained with and without accounting for the smooth group halo. As apparent in the figure, including the smooth group halo in our analysis does not affect the maximum likelihood contours. When the halo is accounted for, we find $\sigma_* = 250^{+141}_{-69}$ km s^{-1} and $s_* = 48^{+117}_{-39}$ kpc. For comparison, when the smooth halo is not accounted for, the best fitting dark matter halo is given by $\sigma_* = 250^{+108}_{-60}$ km s^{-1} and $s_* = 54^{+117}_{-39}$ kpc. As will be discussed in Chapter 6, further research needs to be done before we can conclude these results are consistent with no smooth halo.

5.3 Halo-to-Stellar Mass Ratio

Using the mean tangential shear within 0.5 Mpc, we have already obtained one estimate of average dark matter halo mass for the CNOC2 field and GEEC

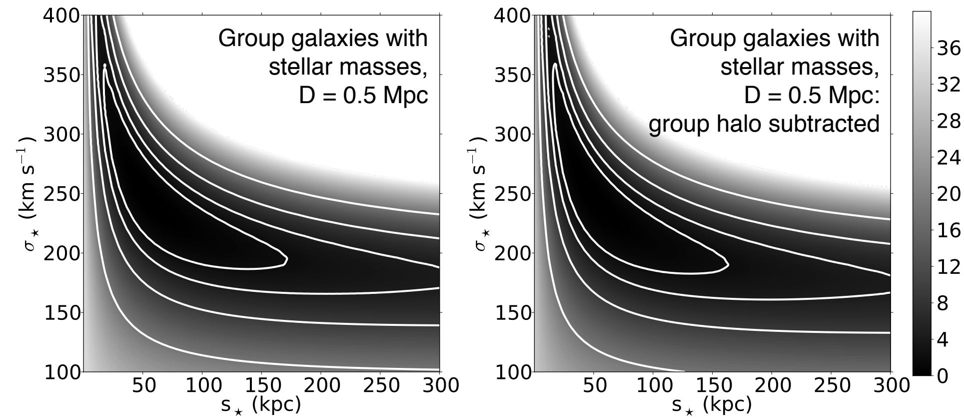

Figure 5.6: Comparison of maximum likelihood contours with (right panel) and without (left panel) taking the smooth group halo into account. Subtracting the smooth group halo has little effect on contours, indicating that the smooth halo contributes little to the weak lensing signal. In both cases, analysis was performed on GEEC group galaxies with stellar masses and imposing a physical separation on lens-source pairs, $D = 0.5$ Mpc.

group galaxies. A second estimate can be determined from the basic stacking analysis, by calculating the mass within $\theta_{max} = 2'$ for a singular isothermal sphere (equation 1.2). Providing constraints are obtained on both σ and s from the maximum likelihood contours, a third estimate of total halo mass can be obtained using equation (1.5). The dark matter halo masses and dark matter-to-stellar mass ratios calculated through these various estimates are summarized in Table 5.3.

It is apparent the estimate of total mass obtained through the maximum likelihood technique is smaller than those obtained through the total mean shear and basic stacking methods. This is caused by the truncation of the dark matter profile used in the maximum likelihood technique. Since the other methods use singular isothermal sphere profiles, which are infinite in extent and therefore mass, they overestimate the mass of the group and field galaxies alike. For these methods, we can obtain more accurate mass estimate by assuming a truncation radius s and adopting a truncated isothermal sphere mass model. For this purpose, we adopt the truncation radius from Hoekstra et al. (2004); $s = 185^{+03}_{-28}\ h^{-1}$ kpc. Nevertheless, in Chapter 6 we restrict our discussion to estimates of total mass obtained through the maximum likelihood method only.

	Field Lenses	**Group Lenses**
Mean Stellar Mass:		
$M_\star$ ($M_\odot$)	9.04×10^9	1.76×10^{10}
Mean Shear within 0.5 Mpc		
Mass within 0.5 Mpc:		
σ (km s^{-1})	81 ± 55	185 ± 40
M_{halo} ($M_\odot$)	1.53×10^{12}	7.96×10^{12}
$M_{halo}/M_\star$	169	452
Total Mass (assume $s = 185\ h^{-1}$ kpc):		
M_{halo} ($M_\odot$)	1.27×10^{12}	6.61×10^{12}
$M_{halo}/M_\star$	140	376
Basic Stacking Method		
Mass within $2'$:		
σ (km s^{-1})	96 ± 28	198 ± 29
M_{halo} ($M_\odot$)	2.48×10^{12}	1.06×10^{13}
$M_{halo}/M_\star$	274	602
Total Mass (assume $s = 185\ h^{-1}$ kpc):		
M_{halo} ($M_\odot$)	1.78×10^{12}	7.57×10^{12}
$M_{halo}/M_\star$	196	430
Maximum Likelihood Technique		
Total Mass:		
σ (km s^{-1})	226^{+135}_{-69}	214^{+45}_{-33}
s (kpc)	18^{+39}_{-15}	72^{+52}_{-30}
M_{halo} ($M_\odot$)	6.71×10^{11}	2.41×10^{12}
$M_{halo}/M_\star$	74	137

Table 5.3: Comparison of the stellar masses, halo masses and halo-to-stellar mass ratios for the CNOC2 field and GEEC group galaxies. Halo mass was determined three ways; by calculating the total mean shear (mass within 0.5 Mpc), using the basic stacking best-fit σ (mass within $\theta = 2'$), and using the maximum likelihood best-fit σ and s (total mass). The mean tangential shear and basic stacking methods appear to be overestimating mass due to the un-truncated halo model. We can adjust for this by assuming a truncation radius, and applying a truncated isothermal sphere mass model. This allows us to estimate of total mass.

Bibliography

Hoekstra, H., Yee, H. K. C., & Gladders, M. D. 2004, ApJ, 606, 67

Wilman, D. J., Balogh, M. L., Bower, R. G., Mulchaey, J. S., Oemler, A., Carlberg, R. G., Morris, S. L., & Whitaker, R. J. 2005, MNRAS, 358, 71

Chapter 6

Discussion & Conclusions

The goal of this work was to investigate how the galaxy group environment affects the dark matter haloes of member galaxies. Using weak galaxy-galaxy lensing we first attempted to detect a truncation of group galaxy dark matter haloes relative to field galaxies. Second, we sought to determine how dark matter is distributed within groups themselves. From these weak lensing analyses, we estimated the dark matter halo mass of group and field galaxies. Our hope was to, third, combine these with stellar mass estimates to determine how the group environment affects the ratio of dark matter-to-stellar masses.

6.1 Truncation of Group Galaxy Haloes

Unfortunately, our current analysis is insufficient to compare the truncation radii of the GEEC group and CNOC2 field galaxies. While we were able to constrain the velocity dispersion σ_* and truncation radius s_* for the GEEC group galaxies, results from the CNOC2 field galaxies were found to be unreliable. This prevents us from making a relative measure of the truncation radius of group galaxies compared to field galaxies.

We believe the CNOC2 field galaxies cannot be constrained for one of two reasons; either our adopted dark matter halo is not ideal, or there are remaining systematics in the data. In the future, we will investigate the field sample more thoroughly before repeating our analysis. In particular, we will investigate how results change when stricter redshift separation between lens and source galaxies is adopted. We will additionally identify sources with poorly defined shapes and lenses with poorly defined magnitudes, and remove these from our analysis. We will also increase our sample size by incorporating the additional two fields of CNOC2 data. In this way, by removing bad lens/source galaxies and adding more data, it may be possible to constrain σ_* and s_* for the field galaxies to reasonable values.

Another issue warranting further investigation is the luminosity scaling. For this work, we adopted $\mu_R^* = -20.42$ based on work by Lin et al. (1999). However, this value may not be appropriate for our data and, with the maximum likelihood technique, it is unclear how luminosity scaling is affected by the value of μ^*. Ideally, we would like to measure μ^* directly from the luminosity function for our sample.

Our analysis of group galaxies was conducted using two of the four CNOC2 fields. For this sample, we find the best-fit dark matter halo has a velocity dispersion of $\sigma_* = 250^{+108}_{-60}$ km s^{-1} using the maximum likelihood technique and $\sigma_* = 223 \pm 33$ km s^{-1} using the basic stacking method. These values are surprisingly large, but they agree within error. The maximum likelihood technique was also used to constrain truncation radius; in our analysis, we found $s_* = 54^{+114}_{-39}$ kpc for the GEEC group galaxies. Although we cannot compare this result against our sample of CNOC2 field galaxies, we can use results from previous work to comment on truncation. Limousin et al. (2007), for example, find the radial extents of dark matter haloes in the cluster environment to be $\lesssim 50$ kpc, consistent with our results. In the field, Hoekstra et al. (2004) find $s_* = 185^{+30}_{-28}\ h^{-1}$ kpc. The truncation radius of our GEEC group galaxies is marginally distinct from this result, indicating truncation of our GEEC group galaxies relative to field galaxies. However, it is important to note that this detection is preliminary. Hoekstra et al. (2004) adopted a different value of μ^* than used in this work. In order to accurately compare our results, we must therefore repeat our analysis adopting the same luminosity scaling as Hoekstra et al. (2004). By incorporating the remaining two CNOC2 fields in future analysis, it may possible to more tightly constrain s_*. This might allow us to determine whether, as predicted, group galaxy dark matter haloes extended relative to cluster galaxies. In addition, with tighter constraints on s_*, we could comment more strongly the truncation of group galaxy dark matter haloes relative to field galaxies.

Recently, Pastor Mira et al. (2011) used weak galaxy-galaxy lensing of numerical simulations to argue that dark matter haloes are not likely to become truncated in the cluster environment. Rather, the tidal forces and tidal heating experienced by an infalling galaxy act together to decrease the central density of its dark matter halo. In this same vein, weak galaxy-galaxy lensing could be used to investigate whether the group environment affects the central density member galaxies, rather than the truncation radius. This could be done by applying a NFW profile to both the CNOC2 field and GEEC group galaxies, and determining if concentration varies between the two environments. In practice, however, this measurement would require a higher density of sources than obtainable with ground based observations. Since the images are much deeper, HST data would be ideal for this purpose.

6.2 Distribution of Dark Matter

While the majority of dark matter in a galaxy cluster is contained within the smooth halo, it is not clear whether this is true of galaxy groups. One goal of this work was to use the maximum likelihood technique to determine how dark matter is distributed within a galaxy group. If the majority of dark matter within a group is contained within the smooth group halo, we expect that the maximum likelihood contours should tighten when the smooth halo is accounted for.[1] As shown in Figure 5.2, accounting for the smooth halo was found to have no effect on the maximum likelihood contours of the GEEC group galaxies. When applying a physical separation cut of 0.5 Mpc on lens-source pairs, the best-fit group galaxy dark matter halo was given by $\sigma_* = 250^{+108}_{-60}$ km s^{-1}, $s_* = 54^{+117}_{-39}$ kpc without the smooth halo included, and $\sigma_* = 250^{+141}_{-69}$ km s^{-1}, $s_* = 48^{+117}_{-39}$ kpc with.

Before we can draw conclusions from this analysis, we must take into consideration the distance of member galaxies from the group centre. The tangential shear induced by the smooth group halo will depend strongly on the location in the galaxy group. If, for example, a source galaxy with $z_S = 1$ is projected 100 kpc from the centre of a galaxy group with a velocity dispersion

[1] Ideally, we would simultaneously fit to the smooth group halo and galaxy subhaloes. Our dataset unfortunately is not large enough for this.

of 300 km s^{-1} and $z_L = 0.3$, the induced tangential shear will be $\gamma_t = 0.034$. However, the average distance of our group members from the group centre is closer to 1 Mpc. At this projected distance, $\gamma_t = 0.003$, and the group halo will contribute little to tangential shearing of distant source galaxies. Since the group halo contribution will increase as distance from the group centre decreases, in future work we will focus our analysis on member galaxies laying within the virial radius of the group. In this way, we hope to detect both the group halo and galaxy subhalo contributions to tangential shear.

Given a larger data sample, it would be possible to similarly investigate the distribution of dark matter with the basic stacking method. Möller et al. (2002) used numerical simulations of galaxy groups (based on the CNOC2 groups from Hoekstra et al., 2001) to analyze how tangential shear profiles are affected by the distribution of dark matter. The authors varied the fraction of dark matter contained within the smooth group halo compared to the galaxy subhaloes, and found the peak value of the tangential shear profile to vary by a factor of ~ 2 (see their Figure 6). In the absence of a smooth group halo, the peak value of tangential shear reaches ~ 0.03. In contrast, in the absence of galaxy subhaloes - i.e., when all dark matter is contained within the smooth group halo - the peak value of tangential shear is $\lesssim 0.01$. The ampliitude of the galaxy tangential shear profile was found to increase as the fraction of dark matter in the galaxy subhaloes increases.

Unfortunately, our sample of GEEC group galaxies was too small to compare against the dark matter distribution models examined by Möller et al. (2002). Our data cannot eliminate any of the distribution models. In order to make use of the results of Möller et al. (2002), we require a far greater density of sources within $20''$ of our lens galaxies.

6.3 Halo-to-Stellar Mass Ratio

One goal of observational cosmology is to relate the observable properties of galaxies to the dark matter haloes in which they reside. The ratio of halo-to-stellar mass, $M_{halo}/M_\star$, represents one way through which this may be possible. Leauthaud et al. (2011) recently investigated how $M_{halo}/M_\star$ depends on $M_\star$. As shown in the bottom panel of Figure 6.1, different systems occupy different regions in the $M_\star$ - $M_{halo}/M_\star$ parameter space. Dwarf galaxies, for example, are dark matter dominated systems with relatively low luminosities. They have hight mass-to-light ratios, and hence large $M_{halo}/M_\star$. Dwarf galaxies would be located on the far left of this plot. Galaxy clusters and groups, on the other hand, are located on the far right, with $M_{halo}/M_\star$-values from a hundred to a thousand.

Individual galaxies occupy the middle of this relation. We would like to determine whether field and group galaxies are located at different points. Since the group environment has been found to quench star formation (Wilman et al., 2005), group galaxies should on average have larger $M_{halo}/M_\star$ relative to field galaxies at a given $M_\star$. In our maximum likelihood analysis of the GEEC group galaxies and CNOC2 field galaxies, we estimated $M_{halo}/M_\star$ to be 137 and 74 in the two environments, respectively. This is consistent with predictions. However, accurate comparison between group and field galaxies cannot be made at this point because the two samples have different stellar mass distributions. Ideally, we would like to measure $M_{halo}/M_\star$ in several narrow bins in $M_\star$. This would then allow us to determine whether group and field galaxies lay in different portions of Figure 6.1.

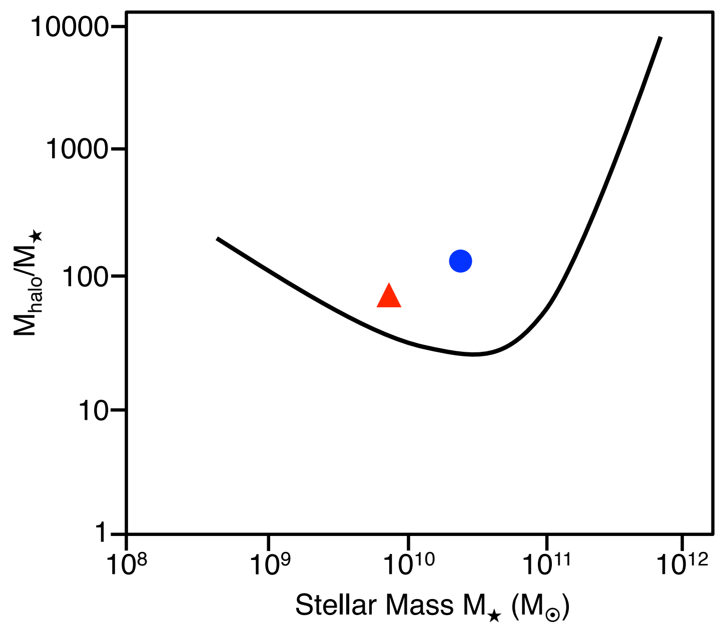

Figure 6.1: The halo-to-stellar mass ratio $M_{halo}/M_\star$ as a function of stellar mass, as measured by Leauthaud et al. (2011) (see their Figure 10). Different systems occupy different parts of the curve; dwarf galaxies are located on the far left, galaxies somewhere in the middle, and galaxy groups and clusters toward the far right. The $M_{halo}/M_\star$ value at the lowest point is ~ 27. We would like to determine whether group galaxies and field galaxies are located at different points. Tentative results for the CNOC field (red triangle) and GEEC group (blue circle) galaxies are shown. Note that these points have not been measured in the same narrow stellar mass bin, and therefore cannot be used to accurately compare the locations of field and group galaxies.

6.4 Summary

Galaxy groups represent a distinct density environment between relatively isolated field galaxies and rich galaxy clusters. The recent availability of large group catalogues, such as the GEEC, have allowed many observable properties of groups and group galaxies to be studied in detail. Relatively, little is known about the dark matter distribution within the group environment. With this work, we hoped to address three the questions regarding the dark matter haloes of galaxies in groups:

1. Are the dark matter haloes of group galaxies truncated relative to field galaxies?
2. Do group and field galaxies have distinguishably different halo-to-stellar mass ratios?
3. Within a galaxy group, how is much dark matter is contained within the galaxy subhaloes, relative to the smooth group halo?

Using weak galaxy-galaxy lensing, we were able to:

1. measure the radial extent of our sample of GEEC group galaxies. We detected a marginal truncation of our group galaxy dark matter haloes compared to field galaxies in previous work. To confirm this result, further research is required with careful comparison between our method and that of the authors we are comparing with. Larger data samples with better galaxy shape measurements also might allow us to decrease the uncertainty in our measurement.

2. calculate initial $M_{halo}/M_{\star}$-values for the GEEC group and CNOC2 field galaxies. Since these samples have different stellar mass distributions, we cannot yet compare the rations of group and field galaxies. Again, larger samples of data are required.

3. develop a method by which the distribution of dark matter in groups can be investigated in the future. Our present analysis was not focused on the inner regions of the group halo, and therefore could not detect the contribution of the smooth group halo to the weak galaxy-galaxy lensing signal. In the future we will restrict our analysis to only those galaxies that lay within, for example, the viral radius of the group centre.

This research is very much a work in progress. In particular, we need to examine the maximum likelihood analysis in greater detail, and robustly study the sample of CNOC2 field galaxies. We are nonetheless optimistic that with further analysis and larger data catalogues we could answer the above questions.

Bibliography

Hoekstra, H., Franx, M., Kuijken, K., Carlberg, R. G., Yee, H. K. C., Lin, H., Morris, S. L., Hall, P. B., Patton, D. R., Sawicki, M., & Wirth, G. D. 2001, ApJ, 548, L5

Hoekstra, H., Yee, H. K. C., & Gladders, M. D. 2004, ApJ, 606, 67

Leauthaud, A., Tinker, J., Bundy, K., Behroozi, P. S., Massey, R., Rhodes, J., George, M. R., Kneib, J.-P., Benson, A., Wechsler, R. H., Busha, M. T., Capak, P., Cortes, M., Ilbert, O., Koekemoer, A. M., Le Fevre, O., Lilly, S., McCracken, H. J., Salvato, M., Schrabback, T., Scoville, N., Smith, T., & Taylor, J. E. 2011, ArXiv e-prints

Limousin, M., Kneib, J. P., Bardeau, S., Natarajan, P., Czoske, O., Smail, I., Ebeling, H., & Smith, G. P. 2007, A&A, 461, 881

Lin, H., Yee, H. K. C., Carlberg, R. G., Morris, S. L., Sawicki, M., Patton, D. R., Wirth, G., & Shepherd, C. W. 1999, ApJ, 518, 533

Möller, O., Natarajan, P., Kneib, J.-P., & Blain, A. W. 2002, ApJ, 573, 562

Pastor Mira, E., Hilbert, S., Hartlap, J., & Schneider, P. 2011, A&A, 531, A169+

Wilman, D. J., Balogh, M. L., Bower, R. G., Mulchaey, J. S., Oemler, A., Carlberg, R. G., Morris, S. L., & Whitaker, R. J. 2005, MNRAS, 358, 71